

MIT Open Access Articles

Visible spectroscopy from the Mission Accessible Near-Earth Object Survey (MANOS): taxonomic dependence on asteroid size

The MIT Faculty has made this article openly available. **Please share** how this access benefits you. Your story matters.

Citation: Devogèle, Maxime, et al., "Visible spectroscopy from the Mission Accessible Near-Earth Object Survey (MANOS): taxonomic dependence on asteroid size." *Astronomical journal* 158, 5 (2019): no. 196 doi 10.3847/1538-3881/AB43DD ©2019 Author(s)

As Published: 10.3847/1538-3881/AB43DD

Publisher: American Astronomical Society

Persistent URL: <https://hdl.handle.net/1721.1/124532>







Version: Final published version: final published article, as it appeared in a journal, conference proceedings, or other formally published context

Terms of Use: Article is made available in accordance with the publisher's policy and may be subject to US copyright law. Please refer to the publisher's site for terms of use.





Visible Spectroscopy from the Mission Accessible Near-Earth Object Survey (MANOS): Taxonomic Dependence on Asteroid Size

Maxime Devogèle¹ , Nicholas Moskovitz¹ , Audrey Thirouin¹ , Annika Gustaffson², Mitchell Magnuson²,
Cristina Thomas² , Mark Willman³, Eric Christensen⁴, Michael Person⁵, Richard Binzel⁵, David Polishook⁶, Francesca DeMeo⁵,
Mary Hinkle², David Trilling² , Michael Mommert¹ , Brian Burt¹, and Brian Skiff¹

¹Lowell Observatory, 1400 W. Mars Hill Road, Flagstaff, AZ 86001, USA; mdevogele@lowell.edu

²Department of Physics and Astronomy, Northern Arizona University, Flagstaff, AZ 86011, USA

³University of Hawaii, Kalaoa, HI, USA

⁴University of Arizona, Department of Planetary Sciences, Lunar and Planetary Lab, Tucson, AZ 85721, USA

⁵Department of Earth, Atmospheric, and Planetary Sciences, Massachusetts Institute of Technology, 77 Massachusetts Avenue, Cambridge, MA 02139, USA

⁶Faculty of Physics, Weizmann Institute of Science, Rehovot 7610001, Israel

Received 2019 February 25; revised 2019 July 27; accepted 2019 August 30; published 2019 October 23

Abstract

The Mission Accessible Near-Earth Object Survey (MANOS) aims to observe and characterize small (mean absolute magnitude $H \sim 25$ mag) Near-Earth Objects (NEOs) that are accessible by spacecraft (mean $\Delta v \sim 5.7 \text{ km s}^{-1}$) and that make close approaches with the Earth (mean Minimum Orbital Intersection Distance MOID ~ 0.03 au). We present here the first results of the MANOS visible spectroscopic survey. The spectra were obtained from August 2013 to March 2018 at Lowell Observatory’s Discovery Channel 4.3 m telescope, and both Gemini North and South facilities. In total, 210 NEOs have been observed and taxonomically classified. Our taxonomic distribution shows significant variations with respect to surveys of larger objects. We suspect these to be due to a dependence of Main Belt source regions on object size. Compared to previous surveys of larger objects, we report a lower fraction of S+Q-complex asteroids of $43.8 \pm 4.6\%$. We associate this decrease with a lack of Phocaea family members at very small size. We also report higher fractions of X-complex and A-type asteroids of $23.8 \pm 3.3\%$ and $3.8 \pm 1.3\%$ respectively due to an increase of Hungaria family objects at small size. We find a strong correlation between the Q/S ratio and perihelion distance. We suggest this correlation is due to planetary close encounters with Venus playing a major role in turning asteroids from S to Q-type. This hypothesis is supported by a similar correlation between the Q/S ratio and Venus MOID.

Key words: catalogs – minor planets, asteroids: general – surveys

Supporting material: machine-readable table

1. Introduction

Near-Earth Objects (NEOs) are defined by a perihelion distance $q < 1.3$ au. The study of NEOs provides access to objects up to 3 orders of magnitude smaller than the smallest observable Main Belt asteroids (MBAs), where most NEOs are thought to have originated. NEOs are also the most accessible objects to spacecraft in the solar system, enabling detailed study of their physical properties. Since the discovery of (433) Eros in 1898, the number of known NEOs has continuously grown and now reaches over 20,000 objects as of April 2019.

To date, a representative census of NEO physical properties exists only for the largest objects (equivalent diameter $D > 1$ km). They have been studied using various techniques such as time-series photometry (e.g., Krugly et al. 2002; Chang et al. 2015), spectrophotometry (e.g., Mommert et al. 2016; Erasmus et al. 2017; Navarro-Meza et al. 2019), spectroscopy (e.g., Binzel et al. 2004, 2019), radar techniques (e.g., Ostro et al. 2007), and polarimetry (e.g., De Luise et al. 2007; Cellino et al. 2018; Devogèle et al. 2018). However, an equivalent census for sub-km NEOs, which represent more than 95% of the currently known population, does not exist. The goal of this work and the Mission Accessible Near-Earth Object Survey (MANOS) is to address this issue.

MANOS is an observational survey of small (mean $H \sim 25$ mag), mission accessible (mean $\Delta v \sim 5.7 \text{ km s}^{-1}$) NEOs

which experience close approaches to Earth (mean Earth Minimum Orbit Intersection Distance or MOID ~ 0.03 au). Δv in this context is defined as the impulse needed for a spacecraft to maneuver from low Earth orbit to a rendezvous with the asteroid in its orbit. It can be computed for NEOs using the approximation described by Shoemaker & Helin (1978). MANOS provides comprehensive characterization of these objects by performing astrometric, photometric (Thirouin et al. 2016, 2018), and spectroscopic (this work) observations. The first observations started in late 2013 and the project is currently funded by the NASA Solar System Observations program through mid-2020.

The study of small NEOs is of importance for several reasons. It is currently estimated that there are $\sim 10^7$ objects with $D > 10$ m, whereas $\sim 10^4$ have $D > 100$ m (Harris & D’Abramo 2015; Trilling et al. 2017). The increasing numbers at small sizes implies higher probability of a small NEO impacting the Earth on relatively short ($<$ decadal) timescales. To date, only three asteroids (2008 TC3, 2014 AA, and 2018 LA) have been telescopically observed prior to impact and all are smaller than 10 m (Jenniskens et al. 2009; Farnocchia et al. 2016, 2018). Studying objects like these and understanding their physical properties will allow development of efficient mitigation strategies in the case of future life-threatening impacts. In addition, observing small asteroids over long periods of time can allow for the characterization of size-dependent evolutionary processes. Specifically, the Yarkovsky

and Yarkovsky–O’Keefe–Radzievskii–Paddack (YORP) effects (Bottke et al. 2006) can provide important information about asteroid spin, thermal, and/or interior properties (Hanuš et al. 2018). Lastly, small asteroids may have different physical properties than larger ones. Models for size sorting of surface particles via seismic shaking suggest that small bodies can have different surface particle size distributions than larger bodies (Maurel et al. 2017). Efficiency of different regolith formation processes might be size dependent (Delbó et al. 2014), and whether or not small objects are even covered by regolith is still debated. In general, asteroids larger than about 200 m are not found to rotate faster than 2.2 hr (Holsapple 2007), though there are rare exceptions (De Luise et al. 2007; Chang et al. 2016; Polishook et al. 2016). Smaller asteroids however can rotate much faster, with some as rapid as 20 s per cycle (Thirouin et al. 2018). These differences in spin properties indicate that the internal structure of large and small objects could be different. While larger objects are usually considered to be rubble-piles, smaller ones could either be monolithic or possess sufficient internal strength to prevent them from breaking apart due to the centrifugal acceleration imparted by rapid rotation (Rožitis et al. 2014; Polishook et al. 2017b; Hérique et al. 2018).

In this work, we present visible spectra for 210 small NEOs (mean size around $D = 60$ m) observed in the framework of MANOS. The spectra of small NEOs allows us to derive their taxonomic classifications (Bus & Binzel 2002; DeMeo et al. 2009). NEOs primarily originate from the Main Asteroid Belt (Granvik et al. 2018); thus by understanding NEOs we probe the population of small MBAs which are currently inaccessible with current observational techniques. Comparing physical properties across size regimes both within and across populations may provide insight into size-dependent evolutionary processes.

In the next section of this paper we present the observations of our 210 NEOs, the three facilities used for these observations, and our reduction procedure. Section 3 introduces asteroid taxonomy and describes the procedures used in this work. In Section 4 we describe the properties of our sample in terms of absolute H magnitude and equivalent estimated diameter, and discuss their taxonomic distribution. Section 5 is devoted to the discussion of the different biases that might affect our sample. Section 6 is devoted to the discussion of the results obtained by merging our sample with two other visible spectroscopic surveys of NEOs (Perna et al. 2018; Binzel et al. 2019). This allows us to analyze the largest available visible spectroscopic database covering asteroids from kilometer down to meter scales. We will discuss the properties of this sample in terms of the taxonomic distribution as a function of orbital parameters, MOID (Minimum Orbit Intersection Distance), and size.

2. Observations and Data Reduction

The observations presented here were conducted over 5 yr from August 2013 to March 2018 using both 8.1 m Gemini North (Maunakea, Hawaii, USA; MPC code: 568) and South (Cerro Pachón, Chile; MPC code: I11) (Mountain et al. 1994), and Lowell Observatory’s 4.3 m Discovery Channel Telescope (DCT; Happy Jack, Arizona, USA; MPC code: G37) (Sebring et al. 2004). The GMOS-N and GMOS-S (Gemini Multi Object Spectrometer) instruments (Davies et al. 1997) were used at the

Gemini observatories and the DeVeney spectrograph (Bida et al. 2014) was used at the DCT.

All observations were reduced using the same python-based spectral reduction pipeline optimized for asteroid spectral reduction. The pipeline was developed for this project and will be the focus of a future publication and public release. In the first step of the pipeline, each image is bias and flat field corrected. Biases are constructed by taking the median of a series of 5 to 11 zero-second exposures. The flat fields were acquired by uniformly illuminating a screen in the dome. A master flat field is constructed by first removing the spectral response of the lamp by normalizing each column (spatial direction) to the median. To avoid differential spatial variation with wavelength, the median is computed only around the region where the target spectra are located on the science images. Next, a cosmic ray filter is applied. We use the *cosmic.py* python based cosmic detection and removal procedure.⁷ This code is based on the Laplacian cosmic ray detection algorithm by Van Dokkum (2001). For both GMOS instruments a spatial nodding procedure is employed during the observations. This technique involves taking spectral exposures with the target nodded to different spatial locations along the slit, and then subtracting pairs of exposures from one other to remove a majority of the sky background. However, due to changing sky conditions from one exposure to the next, some telluric emission lines remain after pair subtraction. A secondary step of background subtraction is then applied by fitting the residual background on either side of the target to interpolate the value at the location of the spectrum. In the case of the DeVeney spectra, no spatial nodding was used and only the second sky background subtraction method was applied. Each spectrum is then extracted, wavelength calibrated, and combined. The final step consists of dividing the NEO spectrum by the spectrum of a solar analog. The solar analog is observed immediately before or after the NEO and is chosen to match as closely as possible the NEO airmass. During the division step, the spectrum of the solar analog is gradually shifted (shift of the order of $10^{-5} \mu\text{m}$) with respect to the spectrum of the asteroid in order to find the combination which provides the best correction of the telluric lines. Finally the spectrum is binned to a resolution of ~ 200 ($0.003 \mu\text{m}$ bins). The pipeline also determines a spectral taxonomic classification by comparing the final asteroid spectrum with Bus-Demeo templates for each taxonomic class using a chi-square analysis. However, for consistency with previous surveys, the reported taxonomic classification was determined using the M4AST taxonomic classification webservice (Section 3 for more details). Table 5 summarizes all the observations presented in this work.

2.1. GMOS@Gemini

We obtained 178 spectra of NEOs using the Gemini Multi-Object Spectrographs (GMOS) in the long-slit mode at both 8.1 m Gemini North (134 objects) and South (44 objects) telescopes. These instruments provide spectral observations from 0.36 to $0.94 \mu\text{m}$.

In 2017, GMOS-North had a detector upgrade which provided better sensitivity in both the red and blue end of the spectral coverage. The old detector consisted of three

⁷ https://obswww.unige.ch/~tewes/cosmics_dot_py/cosmics.py_0.4/doc/index.html

Table 1
Comparison of the Taxonomic Classification for Objects Observed by MANOS and Other Surveys

Object	Instrument	VIS (This work)	VISIR (This work)	VIS	IR	VISIR
(1036) Ganymed	DeVeny	Sr	Sr	S (2)	Sr	Sr (1)
(1981) Midas	DeVeny	V	V	V (4)	V	V (1)
(3752) Camillo	DeVeny	Sr			Ld (5)	
2008 EZ5	DeVeny	Cg	Sq		X/D (1)	
2010 CF19	GMOS-N	Xc	Xc		C/X (1)	
2013 BO76	GMOS-N	Q	Q		S/Sq/Q (1)	
2013 PJ10	GMOS-N	Sr	Sq		S/Sr (1)	
2014 RC	GMOS-S	Sq	Sq		Sq (1)	
2014 SF304	GMOS-N	Q	Q		Q (1)	
2014 WF201	GMOS-N	Xc	Xe		Ch (1)	
2015 TM143	GMOS-N	Cgh		Cb (3)		
2015 XE	GMOS-N	K		K (3)		

References. (1) Binzel et al. (2019), (2) Binzel et al. (2004), (3) Perna et al. (2018), (4) Binzel et al. (2001), (5) De León et al. (2010).

2048 × 4608 chips arranged in a row. Each of these detectors was an e2v deep depletion device with enhanced blue and red sensitivity. These detectors provided a plate scale of 0".0728 per pixels in the spatial direction and a dispersion of 0.174 nm per pixel for the R150 grating and 0.067 nm per pixel for the R400 grating. The upgraded array uses three 2048 × 4176 Hamamatsu detectors which are each optimized for throughput at their respective wavelength regimes. The new plate scale is 0".0807 per pixel in the spatial direction with a dispersion of 0.193 nm per pixel for the R150 and 0.074 for the R400 grating. The new Hamamatsu detectors were used for six targets observed at Gemini North in this work. In the case of Gemini South, all the spectra presented here were obtained with Hamamatsu detectors similar to those at Gemini North. The differences in resolution, detectors, and/or gratings across instruments had no significant effect on our final asteroid spectra, largely because we re-bin the final spectra by a factor of approximately 30 to decrease resolution and increase the signal-to-noise ratio of our faint targets. Such coarse binning effectively cancels the subtle differences across the instruments and detectors.

All spectra were acquired using the same observing sequence. Each target was observed with 6 × 300 s individual exposures. Both GMOS instruments, either before or after upgrade, are multi-CCD detectors which cause small gaps in wavelength coverage. To obtain continuous wavelength coverage over the full 0.36–0.94 μm range, the grating angle in the instrument was changed to produce a dispersion offset of 10 nm between the first three and last three exposures. For each grating offset, three spatial nods separated by 15" along the slit were used to enable sky background subtraction by taking the difference of pairs of images. Before or after each observation of an NEO target a solar analog standard star was observed using the same observation sequence to correct for the solar spectral component and telluric features. After the first three spectral exposures one flat field was acquired with identical grating angle and telescope pointing as used for the target. Then, a second flat field was acquired using the second grating angle before the final three spectral exposures of the target were obtained. Bias images and arc calibrations using a Ne-Ar lamp were acquired during the day before or after the observations. Two different gratings, 150 (R150) and 400 (R400) lines per mm, were used based on availability on the telescope for a given night.

2.2. DeVeny@DCT

The third instrument we employed was the DeVeny spectrograph at Lowell Observatory’s 4.3 m DCT. The DeVeny spectrograph was first known as the KPNO White Spectrograph at the Kitt Peak National Observatory (KPNO). It was acquired by Lowell Observatory in 1998 and used with the 72" Perkins telescope from 2005 to 2015, after which it was modified and installed on the DCT instrument cube (Bida et al. 2014). The DeVeny spectrograph is equipped with a 2048 × 512 e2v CCD42-10 with 13.5 μm pixels. It was operated using a grating of 150 lines per mm providing a dispersion of 0.43 nm/pixel and covering a spectral range from 0.32 to 1 μm. The same reduction procedure was used for DeVeny data as for GMOS with only a few exceptions: no spectral or spatial nodding was performed when observing and no cosmic ray cleaning was needed during reductions. In total 32 NEOs were observed with this instrument.

2.3. Data Validation

To validate our reduction pipeline and observation strategies, we compared our results with observations acquired with other instruments by other teams (Table 1). We found two objects that were also observed in the visible by the NEOSHIELD2 project (Perna et al. 2018) and six objects that were observed by the MITHNEOS project in the NIR (Binzel et al. 2019). Table 1 summarizes taxonomic classifications in the visible, IR, and visible +near-infrared (VISIR) spectral ranges for the two NEOSHIELD2 objects, the six MITHNEOS objects, and three other objects from the literature.

For the NEOSHIELD2 objects, we find the same taxonomic type for one (K-type; object 2015 XE) while the second, 2015 TM143, was found here to be Cgh versus Cb by NEOSHIELD2. This difference may simply be due to the low quality of our data at short wavelengths, which precludes detection of a spectral downturn short-ward of 0.5 μm that can be taxonomically diagnostic. However, even though these are two different types, they correspond to the same complex.

For the MITHNEOS data, even though these observations were not acquired in the same wavelengths regime as MANOS, we were able to compare our results by constructing a composite VISIR spectrum. In all cases the merging between the red end of the visible (GMOS) and the blue end of the NIR (MITHNEOS) spectra are in very good agreement. Figures 1 shows comparisons between our observations, the MITHNEOS survey using the IRTF telescope, and the SMASSIR survey

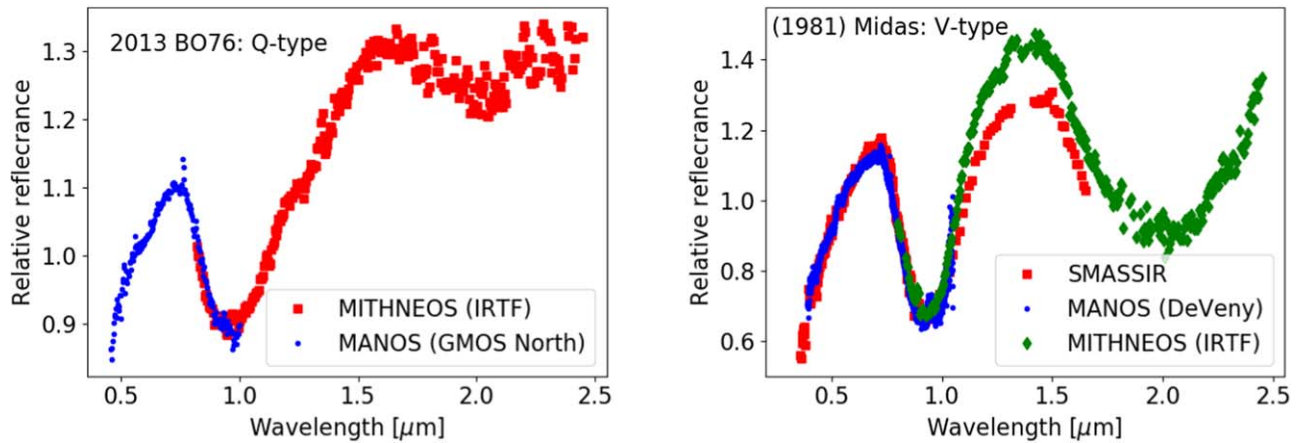


Figure 1. MANOS data validation. Left: comparison between the results from Gemini-GMOS (blue dots) and IRTF-Spex (red squares) in the case of 2013 BO76. Right: comparison between the results from DCT-DeVeny (blue dots), SMASSIR (red squares), and IRTF-Spex (green diamonds) for the case of (1981) Midas.

(Burbine & Binzel 2002). We can see that all data generally agree with one other, though there are some slope differences in the NIR, possibly due to phase angle effects.

Taxonomic classification of VISIR spectra used the MIT classification web service.⁸ For two out of the six MITHNEOS cases (2014 RC and 2014 SF304), we obtain identical classification. For two others (2013 PJ10 and 2013 BO76), Binzel et al. (2019) reported several possible classifications and ours match with one of these. For the last two: 2010 CF19 is found to be within the same complex (X-complex) while 2014 WF201 is fit with two different complexes (Xc for MANOS and Ch for MITHNEOS). In general, these overlapping results across surveys are broadly consistent with one another within the limitations (signal-to-noise, wavelength coverage) of each data set. We note that the more comprehensive VISIR classification can differ from the visible- or IR-only classifications. Thus for the purposes of our analysis and to facilitate consistent comparisons across data sets (Section 6), we only consider from here onwards NEOs classified using visible data only and a single classification technique (Section 3).

As a further validation step for the DeVeny spectrograph and our reduction pipeline, we observed a few well-studied objects (Table 1). For (1036) Ganymed and (1981) Midas we obtained very good agreement with previously published taxonomic classifications (Sr and V respectively). In the case of (3752) Camillo we found an Sr-type asteroid whereas De León et al. (2010) found an Ld-type. However, the NIR data obtained by these authors was not included in their taxonomic assignment and seems to indicate an S-complex object as opposed to an Ld-type. In addition polarimetric data (unpublished by M. Devogèle) indicates an S-type classification. Asteroid 2008 EZ5 is the one object studied here with inconsistent classifications. The composite VISIR spectrum suggests an Sq classification while the individual spectra suggest different classes (Cg for the visible and X or D for the infrared). It is worth noting that the VISIR spectrum, even though classified as a Sq-type, does not match well with the Sq reference, and the near-IR component is relatively low signal-to-noise.

3. Taxonomic Classification

Taxonomic classification is used to group asteroids based on the characteristics of their spectra. There are several taxonomic

classification schemes which have been developed using different data sets covering different spectral ranges and resolutions. Taxonomic classification roughly differentiates between common mineralogical classes present in the asteroid population. Here we make use of the Bus-DeMeo taxonomic classification system (DeMeo et al. 2009), primarily developed for visible plus near-infrared wavelengths (0.45–2.45 μm). Even though our data set does not cover near-infrared wavelengths, the Bus-DeMeo taxonomy is among the most comprehensive and is very similar to the visible-only Bus and Binzel system (Bus & Binzel 2002). Moreover, our spectra go beyond the 0.82 μm limit defining the Bus and Binzel system. In order to make use of the extra wavelength coverage (up to 1 μm for DeVeny), the use of the Bus-DeMeo taxonomic classification system is needed.

For the remainder of this work we will primarily consider just taxonomic complexes as opposed to individual types. This allows better statistics (e.g., more objects per group); moreover, the distinction between types inside a complex is based on subtle spectral variations (slope, shallow absorption bands) that can only be properly resolved in high signal-to-noise spectra, which is not always the case here. We define the S complex as the collection of spectra belonging to the S, Sr, Sv, and Sk-classes. We do not include the Sq class in the S-complex, as done by DeMeo et al. (2009), but rather in a Q-complex combining the Q and Sq-classes as defined by Binzel et al. (2004). The reasons for this are the very high fraction of Q and Sq-types among NEOs compared to the MBA population (objects on which the DeMeo et al. 2014 system was based) and the correlation of Q and Sq-types with low degrees of space weathering (Section 6.1). In addition, we do not include the L, Ld, and K-classes in the S-complex as was done by Binzel et al. (2004), because these types are likely compositionally distinct from the S-complex (Sunshine et al. 2008; Devogèle et al. 2018). The Ld class does not exist in the Bus-DeMeo taxonomy. We combine the K and L-classes into the K complex as these two classes are barely distinguishable at visible wavelengths. NIR data are needed to clearly discriminate these two classes. Finally, we define the C-complex as the group of the B, C, Cb, Cg, Ch, and Cgh-classes, and the X-complex as the group of the X, Xc, Xk, and Xe-classes. In each of these five complexes (S, Q, K, C, X) we have 35, 57, 18, 23, and 50 objects respectively in the MANOS sample. On

⁸ <http://smass.mit.edu/cgi-bin/busdemeoclass.cgi>

Table 2
Taxonomic Distribution of Objects Presented in this Work compared with Those of the NEOSHIELD2 and MITHNEOS Databases

Taxonomy	#	Fraction (%)	#	Fraction (%)	Dev. σ	#	Fraction (%)	Dev. σ
	MANOS		NEOSHIELD2			MITHNEOS		
A	8	3.8 ± 1.3	8	5.5 ± 1.9	+0.7	5	1.7 ± 0.8	-1.3
C (C, Cg, Cgh, Ch, Cb, B)	23	10.9 ± 2.3	14	9.6 ± 2.6	-0.4	34	11.9 ± 2.0	+0.3
D	4	1.9 ± 0.9	10	6.8 ± 2.1	+2.1	13	4.5 ± 1.2	+1.7
K (K, L)	19	9.0 ± 2.1	5	3.4 ± 1.5	-2.2	25	8.7 ± 1.7	-0.1
O	4	1.9 ± 0.9	1	0.7 ± 0.7	1.0	8	2.8 ± 1.0	+0.7
Q (Q, Sq)	57	27.1 ± 3.6	37	25.3 ± 4.2	-0.3	84	29.4 ± 3.2	+0.5
R	2	0.9 ± 0.7	3	2.0 ± 1.2	+0.8	5	1.7 ± 0.8	+0.8
S (S, Sa, Sr, Sv)	35	16.7 ± 2.8	38	26.0 ± 4.2	+1.8	65	22.7 ± 2.8	+1.5
T	4	1.9 ± 0.9	1	0.7 ± 0.7	-1.0	6	2.1 ± 0.9	+0.1
V	4	1.9 ± 0.9	4	2.7 ± 1.4	+0.5	10	3.5 ± 1.1	+1.1
X (X, Xc, Xe, Xk, Xn)	50	23.8 ± 3.4	25	17.2 ± 3.4	-1.4	31	10.8 ± 1.9	-3.3

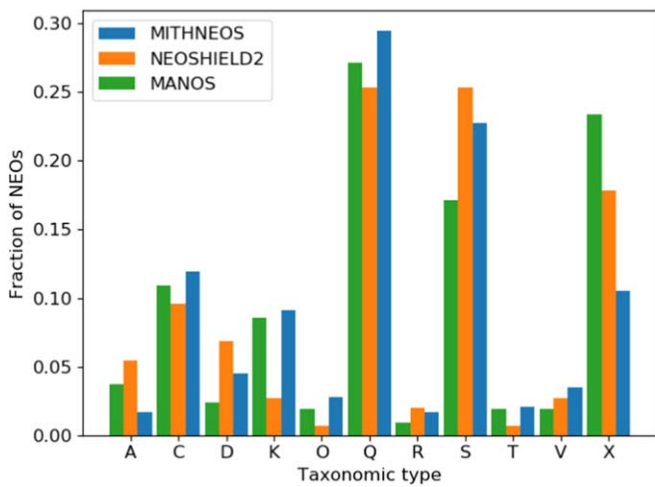


Figure 3. Taxonomic distribution of NEOs in the MANOS, NEOSHIELD2, and chi-squared reclassified MITHNEOS spectroscopic databases in relative percentage. The fraction of S-complex NEOs is lower in the MANOS database while the fraction of X-complex is higher in MANOS and NEOSHIELD2 compared to MITHNEOS.

NEOSHIELD2 data set contains 146 objects with a mean H magnitude of 22 and mean equivalent diameter of 180 m (three times larger than the MANOS sample). The mean H magnitude of the Binzel data set is 17.7 mag corresponding to an equivalent diameter of approximately 1 km (20 times larger than the MANOS sample). These three data sets are highly complementary and sample very different size regimes in the NEO population with MANOS providing the majority of spectra for $H > 23$ or $D < 100$ m. These samples also differ in their orbital element distributions (Section 5). The full combined MANOS+MITHNEOS+NEOSHIELD2 sample contains 642 spectra in roughly equal proportion across the three surveys.

In Table 2, we report the number of spectra and relative fraction in each taxonomic class or complex for each data set. We also report the deviation between our data and the NEOSHIELD2 and MITHNEOS data sets. This deviation corresponds to the fractional difference between the two surveys divided by the uncertainty on this difference computed by uncertainty propagation. The main difference we find is a net decrease in the fraction of S complex NEOs in the MANOS data set. The fraction of S complex asteroids is $22.7 \pm 2.8\%$ in

the MITHNEOS and $26.0 \pm 4.2\%$ in the NEOSHIELD2 data sets while it is only $16.7 \pm 2.8\%$ in MANOS. These numbers correspond to differences compared to MANOS of 1.7 and 1.8 sigma for the NEOSHIELD2 and MITHNEOS data sets, respectively. Hypotheses to explain these differences will be discussed in Section 6.1. In addition, we see a net increase in the fraction of X-complex asteroids with $10.8 \pm 1.9\%$, $17.2 \pm 3.4\%$, and $23.8 \pm 3.4\%$ in the MITHNEOS, NEOSHIELD2, and MANOS data sets respectively. This corresponds to an increase of 2.9 sigma between MITHNEOS and MANOS. X-complex asteroids will be discussed in detail in Section 6.2. The fraction of K-complex in the MITHNEOS survey is comparable with the fraction observed by MANOS while NEOSHIELD2 observed a much smaller fraction. However, due to the very shallow absorption band characterizing the K-complex at visible wavelengths, this result could be related to differences in wavelength coverage between instruments and surveys.

5. Observational Biases

Biases are inherent to any survey, either intentional as with the MANOS focus on small size and low Δv , or unintentional like the discovery bias toward high albedo objects (see Granvik et al. 2018 for a detailed discussion about the discovery bias of NEO discovery surveys). Δv in this context is defined as the impulse needed for a spacecraft to maneuver from low Earth orbit to a rendezvous with the asteroid in its orbit. It can be computed for NEOs using the approximation described by Shoemaker & Helin (1978). In this section we discuss several of these biases to understand their effect on the observed population and taxonomic distribution of NEOs measured by each of the surveys discussed in this work. A more detailed debiasing of our sample will be the focus of a future publication.

5.1. Bias Toward High Albedo

The first bias is a discovery and observational bias toward high albedo asteroids. When observed at visible wavelengths, for similar sizes, high albedo asteroids are brighter and can be more easily discovered and characterized. This bias leads to an observational preference for high albedo classes such as O, A, Q, or S, and under-observation of low albedo classes such as D or C. Discovery bias by the Catalina Sky Survey, currently the predominant NEO discovery survey in the world, has been extensively discussed in Granvik et al. (2018).

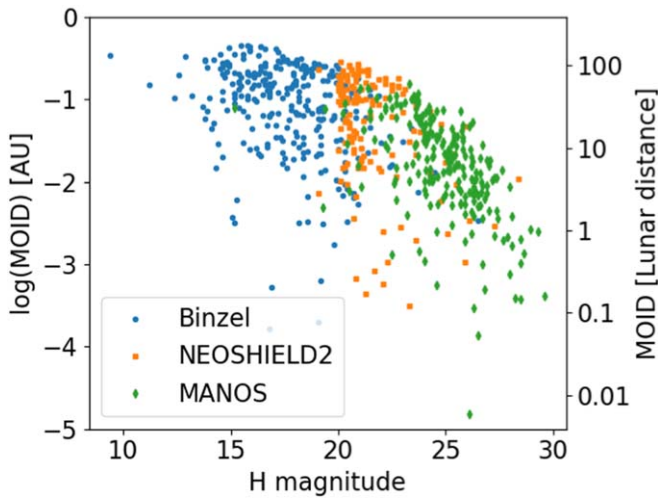


Figure 4. Plot of the absolute H magnitude as a function of the MOID for asteroids in the MITHNEOS, NEOSHIELD2 and MANOS databases. High MOID asteroids are no longer observed as the H magnitude increases.

According to Stuart & Binzel (2004), the de-biased fraction of S-complex NEOs is 22% while MITHNEOS observed $31.8 \pm 3.2\%$ (S+K complexes reported here) and MANOS $25.7 \pm 3.5\%$. We also note that the de-biased fraction of Q complex is estimated to be around 14% while MITHNEOS observed $29.4 \pm 3.2\%$ and MANOS $27.1 \pm 3.6\%$. The S and Q complexes are represented by high albedo asteroids (respectively 0.26 and 0.29 according to Thomas et al. 2011b). On the other hand low albedo classes such as D types ($p_V = 0.02$) have a de-biased population estimated to be around 17% while only $4.5 \pm 1.2\%$ and $1.9 \pm 0.9\%$ were observed by MITHNEOS and MANOS respectively. These statistics clearly show the expected over-observation of high albedo and under-observation of low albedo asteroids.

5.2. Bias Toward Low MOID

Bias toward high albedo is not the only bias present in our sample. MANOS focuses on small objects, which due to their intrinsic faintness are necessarily low MOID objects in order to be observable. This introduces a strong selection effect that biases our observed taxonomic distribution relative to other surveys. The mean MOID for the MITHNEOS, NEOSHIELD2, and MANOS surveys are respectively 0.113, 0.083, and 0.016 au. Figure 4 is a simple illustration of this MOID bias. It shows a plot of the absolute H magnitude as a function of the logarithm of the MOID in au for all asteroids considered in this work. We can clearly see that as H magnitude increases, high MOIDs are no longer observed.

Low MOIDs may have consequences for the surface properties of these asteroids. These asteroids, by definition, are making close approaches to the Earth. These approaches can result in tidal forces that induce surface rejuvenation, effectively suppressing the effects of space-weathering (Binzel et al. 2010). This would then suggest an increase in the fraction of fresh, unweathered spectral types in the MANOS data set. In Section 6.1 we discuss possible reasons for why this is not the case.

5.3. Orbital Elements Biases

The MANOS survey focuses on low MOID, low Δv asteroids. Observing exclusively low Δv asteroids is

introducing a bias toward semimajor axis around $a = 1$ au, low eccentricity e , and low inclination i . This bias can be seen in Figure 5 which shows the semimajor axis a , eccentricity e , and inclination i as a function of the Δv for each survey considered in our analysis. This plot also shows the 90th percentile Δv limits for the different surveys which correspond to $\Delta v = 9.08, 10.78,$ and 6.44 km s^{-1} for the MITHNEOS, NEOSHIELD2, and MANOS surveys, respectively. We can see that by focusing on low Δv objects, MANOS ignores high eccentricity and high inclination targets, while the semimajor axes of our targets are generally closer to that of the Earth compared to other surveys.

The MANOS bias toward Earth-like semimajor axis and low eccentricity naturally introduces a bias toward Earth-like perihelia. Figure 6 represents the perihelion distance of all the objects considered in this work as a function of their Δv . As with Figure 5, the horizontal lines correspond to the 90th percentile Δv lines for the individual surveys. The vertical line corresponds to the semimajor axis of Venus. Note that the 90th percentile Δv of MANOS coincidentally corresponds to the semimajor axis of Venus. This means that MANOS targets have a lower probability of making a close encounter with Venus than objects observed in the other surveys. For example, assuming $a = 1$ au and $i = 0^\circ$, the median Δv for each survey corresponds to minimum perihelia of 0.57, 0.67, and 0.78 au for MITHNEOS, NEOSHIELD2, and MANOS respectively (lower perihelion could be reachable for the same Δv considering lower semimajor axis values; however objects with $a < 1$ only represent 9% of all the objects considered in this work). This bias toward Earth-like perihelia also introduces a bias toward higher Venus MOID in the MANOS sample. The fraction of objects with Venus MOID smaller than 0.02 au is respectively 5.2%, 5.5%, and 0.9% in the MITHNEOS, NEOSHIELD2, and MANOS surveys. Similar to the process that occurs due to Earth encounters Binzel et al. (2010), a low MOID to Venus is expected to increase the likelihood of planetary encounters and thus the chance for surface refreshing events that can affect spectral type. The effect of having a low MOID to Earth and Venus is important while considering the S and Q-complexes. This will be discussed in detail in Section 6.1.

These orbital element biases also introduce a bias toward specific source regions in the Main Belt. Near Earth Asteroids originate from different regions in the Main Belt known to be taxonomically heterogeneous (DeMeo et al. 2014). NEO orbital elements contain a vestige of their original Main Belt source region, thus their escape region probability can be determined (Granvik et al. 2018). Granvik et al. (2018) considered six different escape regions for the Near-Earth Asteroids—the Hungaria and Phocaea clusters, the ν_6 and the Jupiter resonances 5:2, 3:1, and 2:1—and provided the orbital steady state distribution of the NEOs originating from these regions. The MANOS survey is biased toward Earth-like perihelia and low inclination. The Phocaea region is characterized by a relatively small semimajor axis and eccentricity, but has very high inclination ($i \sim 30^\circ$). Since only 5% of the MANOS objects have inclination higher than 14° , objects from the Phocaea region should be very rare in the MANOS sample. On the other hand, 47% and 27% of the objects in the MITHNEOS and NEOSHIELD2 surveys respectively have an inclination higher than 14° . In the case of the MANOS sample, the same bias against Phocaeas is also true for the Hungaria region, but

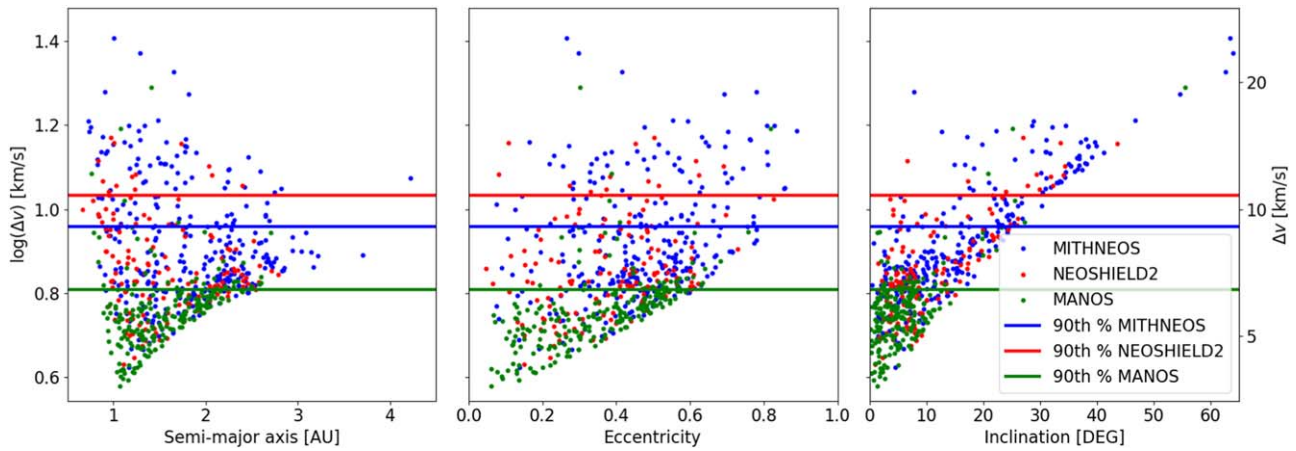


Figure 5. From left to right: plots of the semimajor axis a , eccentricity e , and inclination i as a function of Δv . The different colors represent the different surveys: MITHNEOS (blue), NEOSHIELD2 (red), and MANOS (green). The lines represent the 90th percentile in Δv for each survey (respectively 9.1, 10.8, and 6.4 km s⁻¹). We note that MANOS observed objects in a narrower range of orbital element space ($0.85 < a < 2.6$ au, $e < 0.62$, and $i < 16^\circ$) than the other surveys.

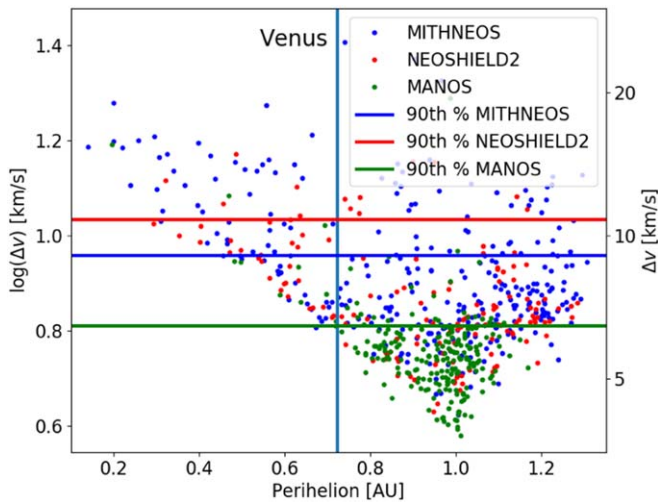


Figure 6. Perihelion as a function of the Δv for each survey (MITHNEOS: blue, NEOSHIELD2: red, and MANOS: green). The horizontal lines represent the 90th percentile of Δv for each survey. The vertical line corresponds to the semimajor axis of Venus $a = 0.723$ au. MANOS only observed targets with perihelia $0.73 < q < 1.17$ au.

to a lesser extent since their inclination is smaller ($i \sim 20^\circ$). The ν_6 , 5:2, 3:1, and 2:1 source regions originate at semimajor axis around 2.2, 2.5, 2.7, and 3.2 au respectively. Thus, at face value, the most likely source region for MANOS targets seems to be the ν_6 resonance: our data set includes only 6.5% of objects with $a > 2.2$ au, 2% with $a > 2.5$ au, and only one object with $a > 2.7$ au. However, the low MOID values characteristic of our sample suggest that MANOS objects may have an increased likelihood to have lost the memory of their source regions due to close interactions with Earth. As such it may be non-trivial to unambiguously determine the source regions for some MANOS objects. A detailed analysis of this issue is beyond the scope of this work.

5.4. Bias Due to Asteroid Size

The main difference between the three surveys discussed in this work is the size of the observed objects. The median H magnitude is respectively 17.5, 21, and 25 mag for the MITHNEOS, NEOSHIELD2, and MANOS samples. The fraction of objects coming from different Main Belt source

Table 3

Fraction, in %, of NEOs Coming from the Different Source Regions According to Granvik et al. (2018) for Targets with H Smaller than 17.5, 21, and 25 mag Corresponding to the Median H for the MITHNEOS, NEOSHIELD2, and MANOS Survey Respectively

Source Region	$H < 17.5$	$H < 21$	$H < 25$
ν_6	39	49	38
3:1J	19	31	36
5:2J	17	12	0.1
Hungaria	11	5	24
Phocaea	7	3	0.02
2:1J	5	2	0.1

regions is dependent on size (Granvik et al. 2018). Table 3 summarizes the fraction of NEOs coming from each source region according to Granvik et al. (2018) for H lower than 17.5, 21, and 25 mag. Even though these statistics are representative of the cumulative distribution, the number of objects in the population increase so quickly with H that for a given H cutoff larger objects become negligible in terms of their contribution to the presented fractions. This can be seen for the Phocaea objects which decrease from 7% to 0.02% for $H < 17.5$ and $H < 25$ mag.

Table 3 indicates that objects from the Phocaea cluster, and the Jupiter resonances of 2:1, and 5:2 are negligible contributors to the MANOS sample, whereas they account for 29 and 17% respectively in the MITHNEOS and NEOSHIELD2 surveys. The main increase in the MANOS sample comes from the Hungaria region which increases by a factor of 2.1 compared to the MITHNEOS sample, and 4.8 compared to the NEOSHIELD2 survey. The 3:1 fraction increases by a factor of 1.9 compared to the MITHNEOS survey and is similar to that for NEOSHIELD2. The ν_6 fraction is similar for MANOS and MITHNEOS, and increases by 10% for the NEOSHIELD2 sample. The taxonomy distribution in each of these source regions is different, and since the contribution of each one is directly dependent on size, the taxonomy distribution of the NEO population should also be dependent on object size. These variations of the taxonomy distribution with size will be discussed in detail in Section 6.1 for the Q and S complexes, and Section 6.2 for the A-type and X-complex.

6. Discussion

In this section the observed variation of the taxonomic distribution in the MANOS database compared to the NEOSHIELD2 and MITHNEOS will be discussed. While combining these three different data sets, trends are also observed as a function of size (H magnitude), MOID, or orbital elements.

The first two sections will focus on specific classes or complexes while the last section will focus on one specific mechanism. Section 6.1 is devoted to the S and Q complexes. The total fraction of S+Q complexes is observed to decrease as a function of size. Mechanisms allowing S to turn onto Q-complex asteroids will be discussed. The Q/S ratio is found to vary as a function the Earth and Venus MOID as well as perihelion distance. Section 6.2 will discuss A-type and X-complex for which a relative increase compare to other taxonomic type/complex is observed as a function of size. The last section is about the size/density dependent disaggregation of asteroids (Scheeres 2018). This mechanism only can possibly explain the overall observed variation of the taxonomy distribution as a function of size.

6.1. S and Q-complex Asteroids

S- and Q-complex asteroids are compositionally related. Q-type asteroids have been linked to the fresh surface of ordinary chondrite meteorites (McFadden et al. 1985; Nakamura et al. 2011). The surface of such an asteroid, when exposed to the space environment, sees its reflectance properties change due to space weathering. For ordinary chondrites, the effects of space-weathering include an increase in spectral slope, a lowering of albedo, and a reduction of absorption band depth. These processes turn Q-types to S-type asteroids (Chapman 1996).

The fraction of S-complex asteroids is significantly lower in the MANOS sample compared to MITHNEOS and NEOSHIELD2. We examine all objects with ordinary chondrite-like compositions by combining the fractions of the S- and Q-complexes which represents 52.1, 51.4, and 43.8% respectively for the MITHNEOS, NEOSHIELD2 and MANOS samples. Figure 7 represents the running mean of the observed S+Q fraction as a function of H magnitude across all three surveys. It can be seen that the S+Q fraction goes from 60% for $H = 16$ mag down to 48% for $H = 17.4$ mag, and 42% for $H = 25$ mag. We also see an interesting peak around $H = 22$ mag with a fraction of 60%. The decrease of the S+Q fraction as a function of H can tentatively be explained by a variation of the source regions of the objects as a function of size. Since the Phocaea asteroids are primarily composed of S-complex asteroids (Carvano et al. 2001) and their abundance among NEOs rapidly decreases with size (Table 3), we expect to find of order 7% less S+Q-complex asteroids for $H < 25$ mag compared to the fraction for $H < 17.5$ mag (assuming Phocaea's are 100% S-complex). This corresponds well to the 8.3% decrease in S+Q asteroids observed in the MANOS sample compared to MITHNEOS. The higher fraction of S around $H = 22$ mag could be explained by the higher fraction of asteroids coming from the ν_6 (10% more than for $H < 17.5$ mag and 11% more than for the MANOS sample). The implication of this interpretation for the non-uniform S+Q fraction is that source regions in the Main Belt can produce taxonomic or compositional variation within the

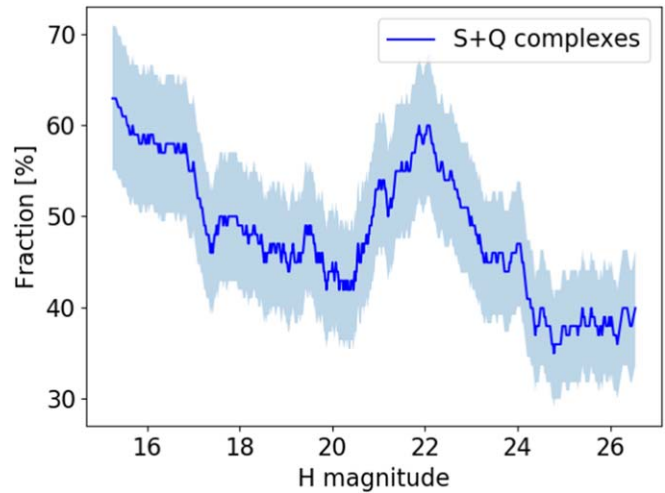


Figure 7. Running mean of the number of S+Q complex asteroids across the MANOS, NEOSHIELD2, and MITHNEOS samples as a function of H magnitude. The shaded area corresponds to the uncertainties taking into account Poisson statistics. This change could be due to size-dependent differences in the Main Belt source region and/or size dependent surface properties like grain size.

NEO population that is size-dependent. Our analysis suggests that this may be an observable signature.

Another tentative explanation for the S+Q fraction trend could be that as body size decreases, surface properties, such as the mean grain size, change. All taxonomic classification systems have been defined based on spectra of MBAs or large NEOs, which are expected to have surfaces dominated by small grain sizes (Robinson et al. 2001; Jaumann et al. 2012) that likely dominate the optical properties at visible and near-infrared wavelengths. Such taxonomic systems may break down when considering significantly different grain size regimes, for example in the nearly regolith-free surface of NEO Ryugu. Evidence for changes in surface grain size as a function of object diameter has been seen with such *in situ* observations of NEOs (Dombard et al. 2010; Tancredi et al. 2015; Michikami et al. 2019). Indirect evidence for the possibility of different surface properties includes the significantly different centripetal accelerations on the surfaces of small objects, where rotation periods less than 20 s have been observed (Thirouin et al. 2018). Such rapid rotation could have implications for the retention of small grains on the surfaces of these bodies. Note that the peak around $H = 22$ mag in Figure 7 closely corresponds to the transition from purely gravity-dominated rubble piles to bodies where cohesion can play a significant role in dictating internal structure and strength (Scheeres et al. 2010). However, it is not clear why a peak in the S+Q fraction would occur at this transition.

Size-dependent changes in surface properties were also predicted by models for objects with low planetary MOID (i.e., those experiencing frequent planetary encounters like in the MANOS sample). These objects can experience gravitationally induced seismic shaking, which can affect surface grain size distributions (Maurel et al. 2017). The implication of these interpretations of the S+Q fraction is that NEOs can have fundamentally different surfaces as a function of size. This can be directly tested with additional *in situ* spacecraft observations of NEOs across a range of sizes, and telescopic observations that can constrain surface grain properties such as measurements of thermal inertia (e.g., Hanuš et al. 2015; MacLennan &

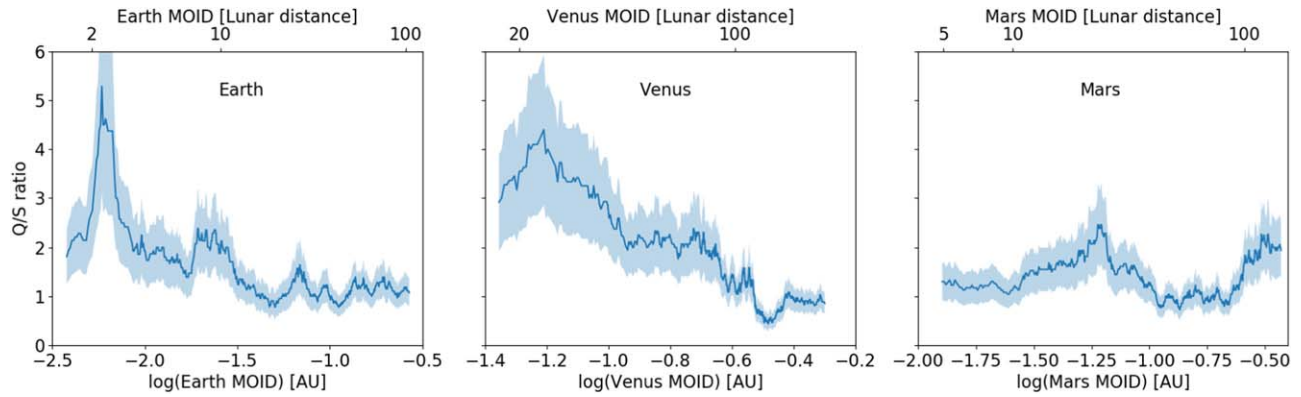


Figure 8. Running mean of the ratio between the number of Q and S asteroids across the MANOS, NEOSHIELD2, and MITHNEOS samples as a function of the Earth, Venus, and Mars MOID (respectively from left to right). The shaded areas correspond to the uncertainties considering Poisson statistics for the S and Q complexes fractions and uncertainties propagation.

Emery 2018) or polarimetric phase curves (e.g., Cellino et al. 2018; Devogèle et al. 2018).

In order to analyze the role of planetary encounters in surface alteration, we consider the Q/S ratio. One model for S-type asteroids to turn into Q-type involves surface re-freshening during planetary encounters (Nesvorný et al. 2005). In order to make a close planetary encounter, an object must have a low MOID relative to the planet. This model is supported by our data since the Q/S ratio for the MANOS survey is $Q/S = 1.6 \pm 0.3$, while it is only 1.3 ± 0.2 and 1 ± 0.2 for the MITHNEOS and NEOSHIELD2 surveys respectively. This is expected because MANOS is biased toward low MOID asteroids. However, these Q/S ratios are only marginally significant in their difference when taking into account uncertainties based on the size of each sample. One can also compare the fractions of Sq and Q sub-type objects (here Q-type is considered as its individual class without taking into account the Sq objects). We see that the Q/Sq ratios for the MANOS, NEOSHIELD2, and MITHNEOS surveys are equal within the uncertainties with respectively 0.8 ± 0.2 , 0.8 ± 0.3 , and 1.1 ± 0.3 .

Figure 8 represents the running mean of MOID, over the full sample, in bin sizes of 100 asteroids as a function of the Q/S ratio for the Earth, Venus, and Mars. In the case of Earth, the Q/S ratio does not go to zero for the highest MOID, but stabilizes around a 1:1 ratio at $\text{MOID} > 0.1$ au. These high MOID asteroids are too distant to experience close encounters with Earth. Including Mars-crosser asteroids in this analysis, the Q/S ratio decreases to 0.33, but does not go to zero. By definition these objects have a MOID larger than 0.3 au and have no interaction with Earth. Either interactions with Mars or some other surface refreshing mechanism that does not involve planetary encounters (e.g., collisional origin in the Main Belt, or YORP spin-up) are likely responsible for the Q-types in this Mars crosser population (DeMeo et al. 2014). We note that while a very close planetary approach (< 1 lunar distance) is actually needed to refresh the surface of an asteroid, this plot only considers instantaneous MOID. As pointed-out by Binzel et al. (2010), Q-type asteroids with MOID as large as 0.15 au can have a MOID as small as 10^{-5} au in the past 10^5 yr. They also noted that not all asteroids with very low MOID in the recent past are Q-types. This fact is relevant to the following discussion on Venus MOID, Mars MOID, and perihelion distance. Considering Q and Sq-type as separate classes, we observe that the Q/S and Sq/S ratio as a function of MOID

distances, for each planet, are well within the error bar associated with each curve. Thus, no differences can be seen between Q and Sq-types. In other words, the Sq/Q ratio remains constant for any MOID within error bars.

Asteroids with high Earth MOID can also have low MOID relative to other planets such as Venus. The effectiveness of a planetary body to refresh an asteroid surface depends on the mass of the planet. This makes Venus nearly as effective as the Earth, while Mars is expected to be much less efficient. The middle panel of Figure 8 represents the running mean of the Q/S ratio as a function of Venus MOID. We can see that as for the Earth the Q/S fraction increases with smaller MOID. We can also see that the increase starts further from the planet than for Earth. This is interpreted as the fact that an asteroid, observable from the Earth, which would have a low Venus MOID, can also have a low MOID relative to the Earth, increasing the probability of planetary encounters. On the other hand, the right hand panel of Figure 8 represents the case of the Mars MOID where no increase of the Q/S ratio is seen. This is consistent with Mars being much less effective than the Earth and Venus in converting S to Q-type asteroids.

Related to these MOID relationships, the Q/S ratio is also dependent on orbital elements. The top left panel of Figure 9 represents the semimajor axis a versus eccentricity e for S and Q-complex asteroids. While the S-complex asteroids predominantly remain near the 1 au perihelion line, a non-negligible fraction of the Q-complex asteroids plot well above this line. The other panels of Figure 9 represent the distribution in semimajor axis (bottom left), eccentricity (top right), and perihelion distance (bottom right) for the S and Q complexes. A Kolmogorov–Smirnov (KS) analysis rejects with 99.9% confidence the null hypothesis that the eccentricity and perihelion distributions of Q and S complex asteroids are drawn from the same distribution (Table 4). On the other hand, the same test for the semimajor axis shows that the null hypothesis can only be rejected with 63% confidence. This means that the distribution of semimajor axis for Q and S is the same, but they are significantly different in terms of eccentricity and hence perihelion as well. Another important observation of Figure 9 is that the relative fraction of S-complex asteroids is rapidly decreasing with lower perihelion distance while the relative fraction of Q-complex is not. This rapid decrease of S-complex objects coincides with perihelion distances inside of Venus’ orbit. This suggests the intriguing

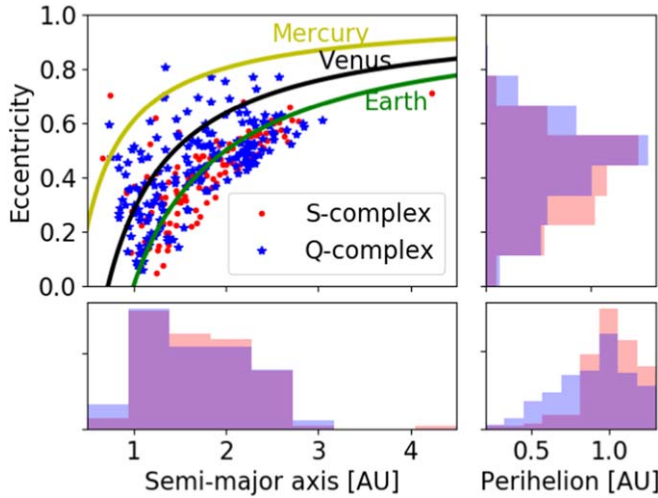


Figure 9. Top left panel: semimajor axis vs. eccentricity plot for S (red dots) and Q-complex (blue stars) asteroids. Lines corresponding to perihelion equal to the semimajor axis of the Earth (1 au), Venus (0.723 au), and Mercury (0.387 au) are displayed in green, black and yellow respectively. Other panels: distribution in eccentricity (top right), semimajor axis (bottom left), and perihelion (bottom right) of the Q (blue) and S (red) complexes. The locations where both histograms overlap are displayed in purple. An excess of Q-complex objects is most pronounced at small perihelion distances.

Table 4

Two-sided KS Probability for Combinations of Perihelion and Eccentricity Distributions from the S-complex (S, Sa, Sr, Sv), Q-complex (Sq, Q), Sq-types (Sq), and Q-types (Q)

	S-complex <i>N</i> = 138	Q-complex <i>N</i> = 178	Sq-type <i>N</i> = 91	Q-type <i>N</i> = 87
Perihelion				
S-complex	0	99.998	99.76	99.99
Q-complex	99.998	0
Sq-type	99.76	...	0	89
Eccentricity				
S-complex	0	99	58	99.9
Q-complex	99	0
Sq-type	58	...	0	94

Note. The numbers represent the probability of rejection of the null hypothesis in %.

possibility that Venus, in addition to the Earth, may play a role in the generation of Q-type asteroids.

The same KS test of comparing the perihelion distribution of the S-complex (*N* = 138) to those of the Sq (*N* = 91) and Q sub-types (*N* = 87) (treated as separate classes) shows that the null hypotheses can be rejected, for both, with a confidence higher than 99%. However comparing the perihelion distribution of Sq with that of the Q sub-type shows that the null distribution can only be rejected with 89% confidence, suggesting that these two distributions are more likely to come from the same population. We also find that the confidence level for rejection is higher when comparing S-complex perihelia to Q-types than when comparing the S-complex to Sq-types. Comparing the eccentricity distributions, we find that the distributions of the S-complex and Sq-type are likely to come from the same population while the populations of the S-complex and Q-type are different. Overall these results are

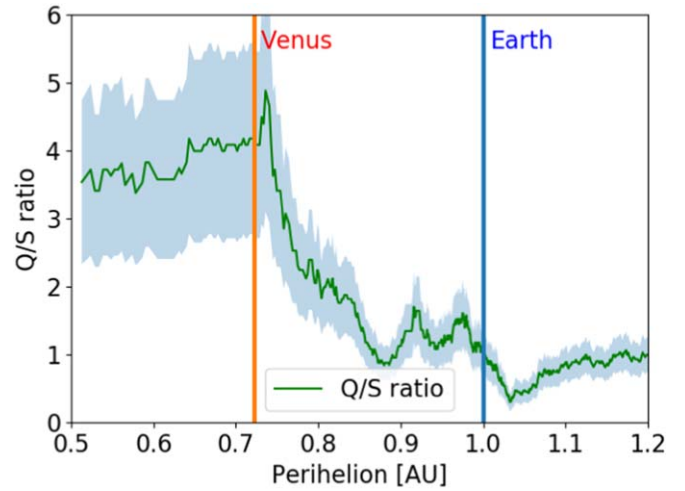


Figure 10. Running mean of the Q/S ratio in 100 object bins as a function of perihelion distance. The shaded areas correspond to the uncertainties considering Poisson statistics for the S and Q complexes fractions and uncertainties propagation. The semimajor axis of the Earth (1 au) and Venus (0.723 au) are shown by blue and red lines respectively. We can see that the Q/S ratio changes slope at perihelion distances around Earth and Venus. We interpret the large increase between Earth and Venus as a mutual influence of both planets modifying surfaces through planetary encounters.

suggestive of a continuous transition from the S-complex to the Sq-type and then to the Q-type as a function of eccentricity and (by extensive) perihelion. In the case of semimajor axis, all distributions are identical.

As such we consider the running mean of the Q/S ratio as a function of perihelion distance (Figure 10). As expected the Q/S ratio increases with lower perihelion. However, this increase is not linear, but has two distinct changes in slope corresponding closely to the perihelion distances of Earth and Venus. We also note that there is a plateau for objects with perihelion between 0.88 and 1 au. These objects encounter Earth, but stay far away from Venus. The maximum Q/S ratio is around 4.9 for perihelia near the semimajor axis of Venus. This suggests that Venus plays a role in the refreshing of S-complex asteroid surfaces. The minimum Q/S ratio is 0.30 at a perihelion distance of 1.03 au, just outside of the Earth’s orbit. The cause of the modest increase in this ratio at perihelion distances greater than 1.03 au is unclear. Mars does not appear to have the same effect that Earth and Venus do in resurfacing objects during close encounters (Figure 8). It is possible that objects recently escaped from the Main Belt are Q-types, for example following collisional removal from a precursor parent body, and thus are affecting the Q/S ratio at larger perihelion distances.

We saw previously that the MANOS survey’s focus on low Δv objects causes a bias against low Venus MOID objects compared to the NEOSHIELD2 and MITHNEOS surveys (Figure 6). As Venus seems to play a role toward increasing the Q/S ratio, this bias should produce a smaller Q/S ratio in the MANOS sample, whereas the MANOS bias toward lower Earth MOID targets should act in the opposite manner. The relative importance of these biases in the MANOS sample remains unclear.

The non-zero Q/S ratio for asteroids which do not interact with Earth or Venus could be explained in several ways:

1. MOID is not a static value but instead evolves with time. Asteroids with a large MOID to Venus and Earth today

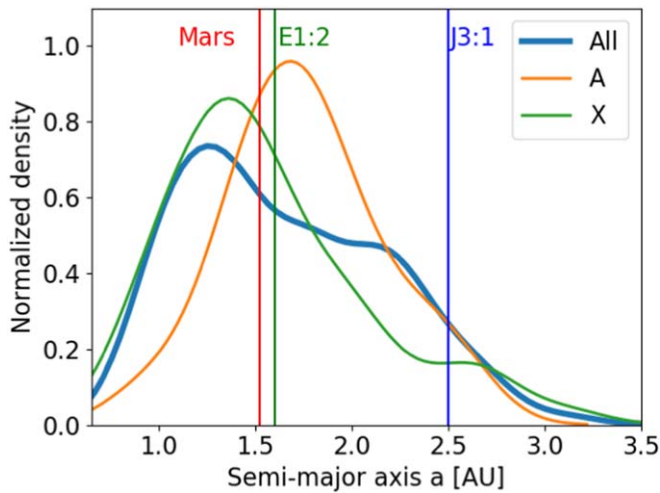


Figure 11. Density distribution of NEOs for the A-types and X-complex as a function of semimajor axis. The red vertical line corresponds to the semimajor axis of the orbit of Mars. The green and blue vertical lines correspond to the location of the 2:1 Earth and 3:1 Jupiter mean motion resonances.

might have had much lower MOIDs in the past. Backwards orbital integrations, similar to those performed by Binzel et al. (2010), could lend insight into this possibility, but is beyond the scope of this work.

2. The fresh Q-type surfaces could come from a collision with another asteroid. However, the collision probability in near-Earth space is much lower than in the Main Belt. Asteroids would then have to enter NEO space as Q-types instead of S-type. A counter would be that very few Q-complex objects have been found in the MBA, though the studied size regimes are very different. Spectra for MBAs are mainly for objects with $D > 5$ km while most of the NEOs have $D < 5$ km. It was also found that small objects from recent dynamical families are more likely to display a fresh Q-type surface (Thomas et al. 2011a).
3. Asteroids can experience spin rate changes due to the YORP effect. This acceleration can cause surface material to migrate toward the equator or even escape the surface (Walsh et al. 2008), thus exposing fresh unweathered terrain. Indeed, some asteroids pairs that were recently formed by the rotational-fission process were found to display fresh Q-type surfaces (Polishook et al. 2014). Combining spectral and rotational data could provide insight into this possibility.
4. Regolith formation processes such as thermal fatigue (Delbó et al. 2014) are expected to be independent of MOID and are also strongly dependent on perihelion distance. This could help to explain the background of Q-complex objects in near-Earth space.

6.2. X-complex and A-type Asteroids

The fraction of X-complex and A-type asteroids increases significantly in the MANOS and NEOSHIELD2 surveys compared to the MITHNEOS survey.

Figure 11 shows the density distribution of objects in the A-class and X-complex as a function of semimajor axis a . The blue curve represents the full data set and serves as a reference. This curve is characterized by a bi-modal distribution with a main peak at 1.275 au and a secondary peak at 2.1 au, corresponding to the inner edge of the Main Belt. There are

only two escape regions with $a < 2.1$ au for objects to leave the Main Belt and enter the NEO population. These correspond to the Hungaria and Phocaea asteroid families. Objects in these families can be destabilized by mean motion resonances with Mars and Jupiter, and to a lesser extent Earth, Venus, and Saturn (McEachern et al. 2010). Several secular resonances such as the ν_5 , ν_6 , or ν_{17} can also play an important role in NEO delivery from these regions (Warner et al. 2009). No significant resonances exist around 1.275 au, whereas the peak at 2.1 au corresponds to a peak of asteroids in the de-biased NEO population (Granvik et al. 2018).

A-type asteroids are uncommon all over the main-asteroid belt. DeMeo et al. (2019) reported fractions of A-types for the inner, mid, and outer main belt to be 0.22%, 0.14%, and 0.11% respectively. These values are more than 10 times lower than those found in the MANOS and NEOSHIELD2 database. However, the fraction of chi-squared classified A-types in the MITHNEOS sample is 4.9 times higher than the fraction of PCA classified A-types. Taking this into account, the PCA classified fraction of A-types in the MANOS sample is estimated to be 0.8 ± 0.3 . This number is more in accordance, however still four times higher, with the estimated fraction of A-type in the Main Belt.

This over-abundance of A-types observed in the MANOS database could be an effect of the observation bias toward high albedo objects. A-types are high albedo (~ 0.3 – 0.5) objects (DeMeo et al. 2019). This effect is expected to be stronger for smaller size objects, which are harder to discover and characterize.

On the other hand, one has to keep in mind that sub-kilometer asteroids cannot be observed in the Main Belt and their fraction cannot be observationally estimated. An indirect estimation by Turrini et al. (2016) suggested that a fraction of 0.7% sub-kilometer A-types in the Main Belt could explain olivine patches detected on the surface of Vesta.

If A-types are distributed more or less evenly throughout the main-belt, some regions in the solar system show over-densities. In that matter, a cluster of 11 asteroids within the fifth Lagrangian point of Mars, was dynamically associated with the asteroid (5261) Eureka, the largest object in the group (Christou 2013). Three of them were found to have A-type spectra (in both the visible and near-IR regime Borisov et al. 2017; Polishook et al. 2017a). Based on the rarity of A-type asteroids, it is likely that these asteroids share a common heritage. Polishook et al. (2017a) suggested this common origin involved impact ejection from Mars. The Hungaria region is also known to display an over-density of A-type asteroids. A recent spectroscopic survey by Lucas et al. (2019) reported a relative A-type fraction of 1.5% in the Hungaria region. Another estimate by DeMeo & Carry (2013) suggested that 7% of the mass of the Hungaria group is of A-type. However more recent studies (DeMeo et al. 2019) suggests a much smaller value of 0.26%.

The A-type population observed in the MANOS survey shows an excess of objects located at semimajor axes around 1.6 au and is associated with a deficiency of objects below 1.3 and over 2.1 au (see Figure 11). The location of this peak corresponds with the 1:2 Earth mean motion resonance which provides the means for Hungaria family asteroids to enter the NEO region.

In addition, the fraction of A-types in the NEO region was found to be size-dependent, increasing with smaller sizes

(Perna et al. 2018). This may be consistent with an increase of the fraction of A-type with smaller size in the main belt (Turrini et al. 2016) or the NEO source region models. As discussed earlier, the relative fraction of Hungaria asteroids in the NEO population increases from 11% for $H < 17.5$ mag to 24% for $H < 25$ mag. This is consistent with an increase of A-types by a factor of 2.3 between the MITHNEOS and MANOS surveys. On the other hand, the predicted fraction of Hungaria NEOs (A-types and others) is only 5% for $H < 21$ mag, which seems inconsistent with the high fraction ($\sim 5\%$) of A-types in the NEOSHIELD2 sample.

Considering these observed properties of A-type asteroids, we suggest that the over-abundance of A-types in NEO space compared to the observed fraction in the Main Belt could be due to either an observation bias toward high albedo asteroids, an increase of the fraction of A-type for unobserved sub-kilometer A-type in the main-belt or a variation of the feeding source region of NEO as a function of size. In the latter scenario A-type NEOs would then be relic pieces of Mars, which is consistent with the fact that Martian meteorites have been found on Earth. The last hypothesis would imply the fact that some asteroids are mistakenly defined as A-type if they are only observed in the visible. DeMeo et al. (2019) found that only half of the A-types defined by the visible regime are actually A-types, when you observe them in the near-IR.

The X-complex, as with the A-types, also shows a strong peak at small a (Figure 11). The Hungaria region is composed of roughly 56% X-type asteroids (Lucas et al. 2019). The X-complex regroups three old taxonomic classes which are distinguished by albedo p_V , but are otherwise spectroscopically similar. P-types are characterized by $p_V < 0.14$, M-types have $0.14 < p_V < 0.30$, and E-types have albedo higher than 0.30 (Tholen 1984). X-types in the Hungaria region are almost exclusively E-type asteroids (Lucas et al. 2019).

From the 106 X-complex asteroids reported in this work, thirteen of them have an albedo measured by NEOWISE. Of these 13, two are consistent with an E-type classification, thus suggesting that 16 ± 11 of the X-complex objects in this study are E-type, representing $2.5 \pm 1.7\%$ of the full sample considered here. From the NEO population with $17 < H < 22$ mag (the X-types for which we have albedo information are exclusively in this range), 5.6% come from the Hungaria region (Table 3). As only 56% of Hungarias are E-type, the expected fraction of E-type asteroids in our sample is 3.1%. This number is consistent with the $2.5 \pm 1.7\%$ suggested by the observations. Specific to MANOS, if the fraction of Hungaria asteroids increases to 24% in the range $17 < H < 25$ mag, as suggested by Granvik et al. (2018), then we might expect to find many more E-types in the MANOS sample. Unfortunately only four MANOS targets have an albedo determination. Of those four, one is an X-type with a high albedo, i.e., is an E-type. A larger sample of small NEO albedos, particularly in the range $22 < H < 25$ mag, would serve to further test this predicted contribution of Hungaria E-types to the NEO population.

We also note that, only the X-types show a significant increase in the MANOS survey: their abundance increases by 61% relative to MITHNEOS. However, the X-complex combines asteroids with a high diversity of albedos, from very dark P-types ($p_V < 0.14$) to very bright E-types ($p_V > 0.30$). The reported mean albedo of X-types by Thomas et al. (2011b) is $p_V = 0.31$, whereas Stuart & Binzel (2004) reported only $p_V = 0.06$. The bias toward observation of high albedo

combined with the increase of high albedo X-type asteroids from the Hungarias region might explain the rapid increasing of X-type while observing smaller asteroids.

6.3. Catastrophic Disaggregation of Asteroids

Several processes leading to full or partial disaggregation of asteroids have been suggested. First, Scheeres (2018) proposed a mechanism leading to the full disruption of small asteroids when reaching a spin rate threshold. The size limit at which such full disaggregation would occur is dependent on density ($R_0 \propto 1/\rho$). On the other hand, the time needed for a body to experience a full disaggregation is also proportional on the density. A low density asteroid will start to disaggregate at larger radius, but would take longer time than a high density one. We also note that $R_0 \sim 100$ m which corresponds to the transition between NEOSHIELD2 and MANOS data. The effect on the observed population of object smaller than 100 m is still unclear, but it might result in variation of the fraction of asteroids of different compositions as a function of size and density.

Taking into account density estimations for the different taxonomic types (Carry 2012), we see that C and S-complex are the lowest density (~ 2.1) while A-type and X and K-complex have relatively higher densities (~ 3.7). For complexes, we report here the mean value of all type belonging to the complex (see Carry 2012 for individual estimation for individual types). These densities have been derived based on large MBAs which might not reflect the true densities of NEOs. However, even if the NEOs possess different macro-porosity due to their smaller size, we are interested here in the relative variation of the density as a function of the taxonomic type and not the absolute values.

If MANOS is observing objects around this transition, then this effect could be a reason for the observed diminution of S-types relative to the higher density X, A, and K-types. Moreover, the size of an object component parts (i.e., boulders) might also be dependant on density, thus also contributing to different taxonomic distributions at small sizes.

The second mechanism involve the catastrophic disruption of asteroids due to solar heating at small perihelion distance (Granvik et al. 2016). This mechanism is also size-dependent, but also albedo, and perihelion distance-dependent.

The catastrophic disruption of an asteroid due to solar heating is expected to happen at perihelion distances too low to affect the MANOS data set which mainly focus on asteroid with perihelion distance close to 1 au. Even if the perihelion distance at which this catastrophic disruption occurs is dependent on the asteroid size, the average disruption distance pass from 0.06 au to 0.18 for H magnitude from 18 to 24, only 8 targets in MANOS data set possess a $q < 0.7$ au. Moreover, the perihelion distribution for high and low albedo asteroids for asteroids with $q > 0.6$ au is found to be similar while it is not considering the full NEO population (Granvik et al. 2016). Even if this analysis was made on large asteroids, this effect is expected to be negligible for Earth-like perihelion MANOS targets.

7. Conclusions

The MANOS project is a survey of small, low Δ_V , low MOID NEOs employing spectroscopic, photometric, and astrometric techniques. As part of this survey we present 210

new visible spectra. The mean H of the MANOS database is around 25 mag which corresponds to a mean equivalent diameter of 50 m. In this paper we presented the taxonomic distribution of these objects.

We compared the taxonomic distribution of the MANOS data set with other data sets of visible NEO spectra (MITHNEOS and NEOSHIELD2). These two surveys sample asteroids that are generally larger than those studied by MANOS. Comparing the taxonomic distribution across surveys we find:

1. The fraction of S-complex asteroids in the MANOS database of $16.7 \pm 2.8\%$ is lower than the fraction in the NEOSHIELD2 and MITHNEOS database which are respectively 26.0 ± 4.2 and $22.7 \pm 2.8\%$. The reason for this decrease is unclear but could be due to an observational selection of lower MOID asteroids in the MANOS sample. The decrease of S-complex could be partially explained by a refreshing of the asteroid's surfaces during close approaches with Earth, Venus, and/or Mars, causing a change in surface features from S to Q-type. This is supported by the fact that the Q/S ratio is increasing in the MANOS database (1.3 in MITHNEOS, 1.0 in NEOSHIELD2, and 1.6 in MANOS).
2. The fraction of S+Q-complex asteroids in the MANOS database of $43.8 \pm 4.6\%$ is lower than the fraction in the NEOSHIELD2 and MITHNEOS database which are respectively 51.4 ± 5.9 and $52.1 \pm 4.2\%$. When combining these data sets this decrease goes from 60% at $H = 16$ mag to 42% at $H = 26$ mag. This could be explained by a decrease in the fraction of asteroids coming from the Phocaea region at small sizes. Another possible explanation would be changes in surface properties (e.g., grain size distribution) as a function of size.
3. The fraction of X-complex asteroids in the MANOS database of $23.8 \pm 3.4\%$ is significantly higher than the fraction in the MITHNEOS database ($10.8 \pm 1.9\%$) and is about the same as in the NEOSHIELD2 database ($17.2 \pm 3.4\%$). This increase of X-complex asteroids is interpreted as both an increase in the fraction of NEOs from the Hungaria family at small sizes ($H > 22$ mag) and a discovery bias toward high albedo E-type asteroids. The high fraction of Hungaria asteroids is supported by the fact that 2 out of 13 X-types with measured albedos are high, consistent with an E-type classification and a Hungaria origin. This seems to support NEO source region models (e.g., Granvik et al. 2018) that predict NEOs of different sizes preferentially come from different parts of the Main Belt. However, this conclusion is based on low number statistics. An albedo survey of X-type NEOs would provide further insight into this scenario.
4. The fraction of A-type asteroids in the MANOS database of $3.5 \pm 1.2\%$ lies between the fraction reported by NEOSHIELD2 ($5.5 \pm 1.9\%$) and MITHNEOS ($1.7 \pm 0.8\%$). This increase compared to the MITHNEOS database is interpreted, like the X-types, as a combination of an increase of NEOs coming from the Hungaria

region at small sizes and a bias toward high albedo objects. These A-types would then potentially be pieces of Mars ejected during the early stages of solar system evolution. This could explain the higher fraction of A-types in the NEO population as compared to that found in the Main Belt.

5. We presented evidence that Venus encounters play a role in the process of turning S-complex into Q-complex asteroids. We also notice that the Q/S ratio is highly correlated with asteroid perihelion distance. This correlation could be due to other physical processes like thermal fatigue which should increase with lower perihelion. However, discontinuities in this ratio are seen around perihelia equal to Earth and Venus, suggesting multiple processes may be at play.

These results made use of the Discovery Channel Telescope at Lowell Observatory. Lowell is a private, non-profit institution dedicated to astrophysical research and public appreciation of astronomy and operates the DCT in partnership with Boston University, the University of Maryland, the University of Toledo, Northern Arizona University and Yale University.

The upgrade of the DeVeny optical spectrograph has been funded by a generous grant from John and Ginger Giovale and by a grant from the Mt. Cuba Astronomical Foundation.

Part of the data utilized in this publication were obtained and made available by the The MIT-UH-IRTF Joint Campaign for NEO Reconnaissance. The IRTF is operated by the University of Hawaii under Cooperative Agreement no. NCC 5-538 with the National Aeronautics and Space Administration, Office of Space Science, Planetary Astronomy Program. The MIT component of this work is supported by NASA grant 09-NEOO009-0001, and by the National Science Foundation under grants Nos. 0506716 and 0907766.

Based on observations obtained at the Gemini Observatory, which is operated by the Association of Universities for Research in Astronomy, Inc., under a cooperative agreement with the NSF on behalf of the Gemini partnership: the National Science Foundation (United States), National Research Council (Canada), CONICYT (Chile), Ministerio de Ciencia, Tecnología e Innovación Productiva (Argentina), Ministério da Ciência, Tecnologia e Inovação (Brazil), and Korea Astronomy and Space Science Institute (Republic of Korea). The authors wish to acknowledge all the astronomers who obtained the data for this work.

The authors acknowledge support from NASA NEOO grants NNX14AN82G, and NNX17AH06G. D. Polishook is grateful to the Ministry of Science, Technology and Space of the Israeli government for their Ramon fellowship for post-docs.

Appendix A Observing Circumstances and Taxonomy for the NEOs Observed by MANOS

Table 5 summarizes all the observations presented in this work.

Table 5
Observational Circumstances and Spectral Analysis Results

Object	<i>H</i> mag	Obs. Date (YY MM DD)	V mag (NEO)	Δ [LD]	Airmass (NEO)	Solar analog (SA)	Airmass (SA)	MOID (au)	Δv (km s ⁻¹)	Phase (deg)	Fac.	Taxon.
1999 SH10	22.5	14 Apr 30	20.5	47.3	1.09	SA107-998	1.23	0.0094	5.5	66.8	GMOSN	V
2004 VJ1	24.3	15 Nov 04	19.6	38.6	1.07	SA93-101	1.08	0.0136	5.2	3.4	GMOSN	Cb
2007 MK6	19.9	16 Jun 15	18.5	39.6	1.12	SA105-56	1.39	0.0878	15.5	89.8	DCT	O
2008 EZ5	19.4	17 Mar 19	17.7	106.7	1.23	SA107-998	1.5	0.0775	6.4	8.3	DCT	Cg
2008 HA2	24.4	15 Mar 02	19.9	28.2	1.17	SA102-1081	1.15	0.0593	5.4	22.6	GMOSS	K
2009 CP5	21.5	13 Aug 16	18.1	38.3	1.07	SA115-271	1.17	0.0579	5.4	35.0	GMOSN	Sq
2010 CE55	22.2	13 Aug 11	20.9	86.8	1.06	SA115-271	1.1	0.0281	4.3	42.4	GMOSN	L
2010 CF19	21.7	13 Aug 12	19.1	57.8	1.27	SA115-271	1.2	0.0327	5.5	26.9	GMOSN	Xc
2011 BN24	20.9	13 Aug 11	19.5	74.1	1.06	SA115-271	1.0	0.0156	5.5	52.4	GMOSN	X
2012 CO46	22.9	17 Sep 14	19.7	64.0	1.17	SA115-271	1.09	0.0893	4.7	8.6	GMOSS	Cgh
2013 BO76	20.4	13 Aug 12	17.2	41.2	1.2	SA113-276	1.06	0.0285	6.3	34.7	GMOSN	Q
2013 PC7	22.4	13 Aug 12	19.0	56.2	1.25	SA113-276	1.32	0.1045	6.5	6.2	GMOSN	Q
2013 PH10	23.3	13 Aug 09	20.4	62.2	1.07	SA112-1333	1.19	0.1543	5.3	13.2	GMOSN	Xe
2013 PJ10	24.7	13 Aug 11	18.6	11.3	1.11	SA113-276	1.02	0.0025	5.0	41.8	GMOSN	Sr
2013 SR	24.1	13 Oct 09	19.8	27.4	1.57	SA115-271	1.22	0.0695	5.3	30.4	GMOSN	Xc
2013 VY13	21.2	13 Dec 11	19.3	115.3	1.35	SA98-978	1.06	0.0422	6.3	1.3	GMOSN	S
2013 WA44	23.6	13 Dec 11	20.7	68.5	1.2	HD28099	1.17	0.0206	4.2	6.1	GMOSN	Sq
2013 WS43	22.8	13 Dec 11	19.4	50.0	1.2	HD28099	1.18	0.0592	5.5	19.0	GMOSN	Sa
2013 XV8	21.8	14 Feb 28	19.0	56.7	1.47	SA102-1081	1.33	0.1044	4.9	25.3	GMOSN	X
2014 DF80	25.9	14 Mar 11	20.7	30.4	1.07	SA102-1081	1.04	0.0718	5.3	4.4	GMOSN	Ch
2014 FA7	26.7	14 Mar 27	20.1	10.7	1.29	SA105-56	1.16	0.0036	5.1	23.8	GMOSN	C
2014 FB44	25.6	14 Apr 07	20.3	15.2	1.11	SA105-56	1.06	0.0161	5.5	45.9	GMOSN	L
2014 FN33	21.1	14 Apr 06	19.6	96.4	1.36	SA107-998	1.4	0.1364	6.5	26.0	GMOSN	Sq
2014 FP47	22.3	14 Apr 07	19.4	65.0	1.11	SA105-56	1.32	0.0257	5.3	11.4	GMOSN	Q
2014 GG49	25.7	14 Apr 13	19.9	15.9	1.1	SA107-998	1.01	0.0077	5.8	22.7	GMOSN	Xe
2014 HE177	25.8	14 May 09	20.2	19.1	1.08	SA105-56	1.32	0.0479	5.9	13.5	GMOSN	C
2014 HK129	20.9	14 May 18	20.7	133.1	1.27	SA105-56	1.14	0.0087	6.2	34.8	GMOSN	A
2014 HS4	26.2	14 Apr 29	20.4	20.5	1.22	SA107-998	1.24	0.0464	5.6	9.2	GMOSN	A
2014 HT46	26.6	14 Apr 30	19.6	8.4	1.09	SA107-998	1.28	0.0127	4.3	30.4	GMOSN	Sa
2014 JD	26.3	14 May 06	19.7	11.2	1.1	SA110-361	1.1	0.0059	6.1	21.5	GMOSN	O
2014 JJ55	25.2	14 May 18	20.1	17.2	1.11	SA107-998	1.1	0.0196	4.9	36.3	GMOSN	Xe
2014 MD6	21.5	14 Sep 24	20.0	85.1	1.11	SA93-101	1.03	0.0721	6.2	35.6	GMOSN	Sv
2014 OT338	21.4	14 Sep 24	20.1	100.0	1.26	181-005382	1.16	0.137	6.0	25.0	GMOSN	Sq
2014 RC	26.8	14 Sep 07	15.5	1.4	1.16	SA113-276	1.08	0.0005	5.8	14.5	GMOSS	Sq
2014 RF11	23.7	14 Sep 21	20.0	38.9	1.44	SA112-1333	1.07	0.0964	5.2	24.9	GMOSS	Sr
2014 SB145	26.3	14 Oct 02	18.7	7.2	1.11	SA93-101	1.07	0.0038	5.0	20.4	GMOSN	C
2014 SF304	27.2	14 Oct 03	17.8	3.2	1.07	SA93-101	1.01	0.0022	4.9	15.3	GMOSN	Q
2014 SO142	24.4	14 Oct 01	20.1	38.0	1.06	SA93-101	1.06	0.0201	6.1	6.9	GMOSN	Xc
2014 SU1	24.8	14 Oct 07	20.2	15.4	1.16	SA93-101	1.21	0.0136	4.1	56.2	GMOSS	Xe
2014 TP57	26.4	14 Oct 21	18.8	8.4	1.09	SA93-101	1.06	0.0202	5.2	17.6	GMOSN	Cb
2014 TR57	25.2	14 Oct 25	20.4	22.5	1.21	SA93-101	1.09	0.0233	5.5	30.8	GMOSN	S
2014 UC115	23.7	14 Dec 18	20.4	48.9	1.41	HD28099	1.06	0.1171	6.1	20.7	GMOSN	Q
2014 UV210	27.0	14 Dec 16	18.7	7.2	1.88	SA98-978	1.3	0.0183	3.9	5.5	GMOSN	Cb
2014 VG2	22.7	14 Nov 24	19.8	42.6	1.18	SA93-101	1.01	0.0146	5.1	45.4	GMOSS	Sq
2014 WC201	26.1	14 Nov 28	18.9	9.4	1.27	HD28099	1.32	0.0024	6.3	13.6	GMOSN	Sq
2014 WE120	23.9	14 Nov 28	19.8	18.8	1.22	SA102-1081	1.2	0.0285	5.0	65.1	GMOSN	O
2014 WE121	23.5	14 Dec 18	20.9	46.3	1.41	HD28099	1.1	0.0763	5.0	47.3	GMOSN	Xe
2014 WF201	25.6	14 Nov 29	18.6	9.2	1.14	HD28099	1.17	0.016	5.1	22.6	GMOSN	Xc
2014 WO69	23.5	14 Nov 24	19.9	49.4	1.26	HD28099	1.14	0.0985	6.2	9.0	GMOSN	S
2014 WP4	24.3	14 Nov 28	19.3	19.6	1.07	SA98-978	1.06	0.0406	6.7	33.9	GMOSN	A
2014 WR6	25.3	14 Nov 24	19.9	18.5	1.26	HD28099	1.06	0.0437	5.5	23.2	GMOSN	Xe
2014 WS7	27.3	14 Nov 22	18.8	4.5	1.19	SA98-978	1.18	0.0111	6.1	26.6	GMOSS	Sr
2014 WX202	29.6	14 Dec 01	19.7	1.0	1.13	SA93-101	1.07	0.0004	3.9	88.4	GMOSN	Q
2014 WX4	26.4	14 Nov 19	19.8	10.7	1.18	SA98-978	1.03	0.0075	5.5	25.3	GMOSN	K
2014 WY119	26.3	14 Nov 26	18.1	4.4	1.18	SA93-101	1.22	0.0086	5.0	39.3	GMOSS	Sq
2014 YD	24.2	14 Dec 20	20.3	25.2	1.43	SA102-1081	1.07	0.0052	4.0	52.2	GMOSN	Xc
2014 YD42	22.3	15 Jan 08	19.8	95.6	1.09	SA98-978	1.0	0.0816	6.9	2.1	GMOSN	L
2014 YN	25.8	14 Dec 22	19.3	10.9	1.01	HD28099	1.1	0.0053	5.7	32.1	GMOSN	Xc
2014 YT34	24.7	15 Jan 08	18.4	15.4	1.09	SA98-978	1.07	0.0354	5.8	11.6	GMOSN	Xe
2014 YZ8	23.7	15 Jan 09	20.6	29.9	1.07	180-113477	1.31	0.0577	6.0	68.5	GMOSN	L
2015 AK1	24.3	15 Jan 14	18.5	13.9	1.11	SA98-978	1.31	0.0143	6.2	33.1	GMOSN	X
2015 AZ43	23.8	15 Feb 16	17.5	7.8	1.23	SA105-56	1.68	0.0014	5.7	71.3	GMOSN	T
2015 BF511	24.6	15 Feb 02	20.4	27.5	1.32	SA102-1081	1.1	0.0053	4.9	28.5	GMOSS	D

Table 5
(Continued)

Object	H mag	Obs. Date (YY MM DD)	V mag (NEO)	Δ [LD]	Airmass (NEO)	Solar analog (SA)	Airmass (SA)	MOID (au)	Δv (km s^{-1})	Phase (deg)	Fac.	Taxon.
2015 BK4	24.9	15 Jan 22	17.9	9.0	1.22	SA102-1081	1.2	0.0064	5.9	24.5	GMOSS	S
2015 BM510	25.1	15 Feb 02	19.5	15.2	1.16	SA98-978	1.08	0.0236	4.8	33.5	GMOSS	D
2015 CF	23.6	15 Feb 16	19.9	41.1	1.07	SA98-978	1.27	0.0629	6.0	24.8	GMOSN	S
2015 CQ13	25.7	15 Feb 17	18.6	6.8	1.13	SA105-56	1.1	0.0056	5.7	44.2	GMOSN	Xe
2015 CW13	22.7	15 Mar 15	19.6	27.6	1.06	SA98-978	1.04	0.006	4.9	70.2	GMOSN	A
2015 CZ12	25.3	15 Feb 16	20.1	27.2	1.07	SA102-1081	1.02	0.0283	5.6	3.6	GMOSN	K
2015 DC54	26.1	15 Feb 22	20.0	13.0	1.07	SA105-56	1.03	0.0076	5.8	27.2	GMOSN	Q
2015 DK200	25.8	15 Mar 03	19.4	11.0	1.17	SA105-56	1.13	0.0148	5.2	38.9	GMOSN	Xc
2015 DO215	26.6	15 Mar 03	18.2	3.1	1.4	SA102-1081	1.22	0.0074	4.7	58.6	GMOSS	A
2015 DP53	24.3	15 Feb 22	19.3	23.0	1.23	SA102-1081	1.06	0.0507	5.6	17.2	GMOSN	S
2015 DS	24.8	15 Feb 25	19.9	19.8	1.18	SA98-978	1.17	0.0429	4.5	34.6	GMOSS	L
2015 DS53	24.0	15 Mar 02	16.4	3.7	1.17	SA102-1081	1.17	0.008	7.3	65.1	GMOSS	Xc
2015 DU	26.6	15 Feb 22	19.3	8.0	1.23	SA102-1081	1.17	0.0194	4.0	23.9	GMOSN	Sq
2015 DZ198	24.6	15 Mar 03	19.6	24.5	1.17	SA105-56	1.13	0.0116	6.0	16.1	GMOSN	Sr
2015 EE7	20.2	15 Apr 12	17.9	44.3	1.25	SA98-978	1.03	0.0677	9.3	65.2	GMOSS	Sq
2015 EF	26.8	15 Mar 11	19.0	9.2	1.21	SA102-1081	1.23	0.0063	6.7	3.4	GMOSS	Sq
2015 EK	26.3	15 Mar 12	18.4	3.8	1.22	SA98-978	1.11	0.0067	5.6	59.0	GMOSS	Q
2015 FC	26.6	15 Mar 24	18.8	5.1	1.07	SA102-1081	1.03	0.0051	5.1	40.9	GMOSN	Xe
2015 FP	25.1	15 Mar 24	18.2	11.6	1.07	SA102-1081	1.04	0.0245	5.5	7.6	GMOSN	Xe
2015 FW33	25.9	15 Mar 23	19.3	9.6	1.14	SA102-1081	1.08	0.0205	4.7	36.0	GMOSN	Sq
2015 FX33	25.8	15 Mar 23	19.8	14.5	1.14	SA102-1081	1.07	0.0342	5.5	25.6	GMOSN	Xc
2015 HS11	27.1	15 Apr 28	19.6	7.6	1.07	SA107-998	1.06	0.0182	4.3	19.4	GMOSN	C
2015 HV11	24.3	15 May 12	19.1	24.2	1.36	SA105-56	1.64	0.0587	6.1	15.1	DCT	V
2015 JF	26.3	15 May 12	19.7	14.0	1.54	SA105-56	1.24	0.0101	5.2	7.3	DCT	Xe
2015 JR	26.3	15 May 12	18.9	5.6	1.75	SA105-56	1.24	0.0087	6.4	45.3	DCT	O
2015 JW	25.8	15 May 20	19.6	18.3	1.39	SA107-998	1.11	0.0314	5.8	3.3	GMOSS	Cg
2015 KA	26.2	15 May 19	18.8	7.7	1.09	SA105-56	1.19	0.0157	6.0	20.8	GMOSN	Sr
2015 KE	26.2	15 May 24	20.4	14.1	1.2	SA105-56	1.21	0.0043	4.5	28.3	GMOSS	S
2015 LQ21	24.4	15 Jun 20	19.0	13.8	1.25	SA110-361	1.3	0.0258	6.1	42.4	DCT	D
2015 MC	24.2	15 Jun 20	18.7	18.6	1.63	SA107-684	1.27	0.0101	5.6	20.8	DCT	Sq
2015 NA14	22.0	15 Jul 26	17.7	24.6	1.06	SA112-1333	1.0	0.0608	5.7	40.5	GMOSN	Sq
2015 OM21	22.5	15 Jul 27	19.5	41.1	1.18	SA115-271	1.07	0.078	6.5	42.6	GMOSN	Q
2015 OQ21	27.9	15 Jul 23	17.8	1.9	1.15	SA110-361	1.4	0.0022	8.7	32.1	GMOSN	V
2015 PK9	23.7	15 Aug 18	18.9	22.3	1.28	SA112-1333	1.19	0.0126	5.8	30.4	DCT	Cg
2015 QB	24.2	15 Aug 18	19.4	23.9	1.22	SA112-1333	1.26	0.0339	5.4	22.6	DCT	K
2015 SA	25.3	15 Sep 19	18.7	8.5	1.26	SA112-1333	1.03	0.0052	8.6	42.8	GMOSN	Q
2015 TD144	22.5	15 Oct 19	17.7	13.3	1.09	HD28099	1.04	0.0013	8.8	67.8	GMOSN	Q
2015 TL238	24.9	15 Oct 22	19.2	19.3	2.1	SA93-101	1.88	0.0277	7.5	13.3	GMOSN	Sq
2015 TM143	23.6	15 Oct 20	19.8	37.8	1.25	SA115-271	1.28	0.0286	5.7	23.0	GMOSN	Cgh
2015 TW237	23.1	15 Nov 10	20.0	57.6	1.17	SA93-101	1.09	0.0926	5.3	10.5	GMOSN	Sr
2015 TZ143	25.9	15 Oct 22	18.6	4.3	1.33	SA93-101	1.12	0.0067	6.7	56.9	GMOSN	Q
2015 TZ237	24.3	15 Oct 21	20.0	28.8	1.18	SA93-101	1.08	0.0727	5.7	30.4	GMOSN	T
2015 VA106	22.7	15 Nov 18	18.4	31.3	1.63	SA93-101	1.12	0.0106	6.2	20.4	GMOSN	Q
2015 VE66	24.1	15 Nov 16	18.0	11.6	1.65	SA93-101	1.63	0.0189	6.0	35.2	GMOSN	Sv
2015 VG105	24.0	15 Nov 15	17.9	17.0	1.16	SA93-101	1.0	0.043	5.8	8.4	GMOSN	C
2015 VN105	27.6	15 Nov 15	19.9	6.0	1.16	SA93-101	1.15	0.0136	6.3	32.4	GMOSN	Xk
2015 VO105	24.0	15 Nov 16	19.7	20.6	1.65	SA93-101	1.2	0.0011	4.8	54.0	GMOSN	Sr
2015 VO142	29.0	15 Nov 21	18.9	2.1	1.63	SA93-101	1.75	0.0026	4.3	30.8	GMOSN	Sq
2015 WA13	26.3	15 Dec 05	18.8	7.6	1.09	HD28099	1.27	0.0177	4.6	28.7	GMOSN	L
2015 XB	24.1	15 Dec 05	18.7	17.4	1.45	SA93-101	1.09	0.0362	8.0	31.0	GMOSN	Xe
2015 XE	26.2	15 Dec 07	19.2	19.7	1.06	SA98-978	1.0	0.0109	4.5	18.1	GMOSN	K
2015 XM128	24.0	15 Dec 28	20.0	23.1	1.35	SA115-271	1.15	0.0311	6.3	67.1	GMOSN	B
2015 XO	26.3	15 Dec 05	20.3	21.7	1.09	HD28099	1.21	0.0536	5.4	4.2	GMOSN	X
2015 YD	24.1	15 Dec 30	19.9	38.2	1.08	SA98-978	1.0	0.0504	5.8	10.1	GMOSN	Sr
2015 YD1	24.4	15 Dec 29	19.7	28.4	1.24	SA98-978	1.27	0.0593	6.8	22.3	GMOSN	L
2015 YE	23.4	15 Dec 31	20.2	53.9	1.13	SA98-978	1.08	0.1017	6.7	16.6	GMOSN	Sq
2015 YS9	25.9	15 Dec 31	19.4	12.5	1.13	SA98-978	1.01	0.004	5.2	14.1	GMOSN	Xe
2016 BB15	24.4	16 Feb 03	20.4	45.5	1.07	SA102-1081	1.04	0.0206	6.0	6.4	GMOSN	Sv
2016 BC15	24.9	16 Feb 04	20.4	30.8	1.28	SA98-978	1.01	0.0748	6.4	12.3	GMOSN	Sq
2016 BJ15	23.5	16 Feb 03	18.5	23.4	1.07	SA102-1081	1.04	0.0163	6.1	28.0	GMOSN	Q
2016 BW14	25.8	16 Feb 04	20.4	19.2	1.28	SA98-978	1.12	0.0415	6.6	23.8	GMOSN	Xc
2016 CF29	24.9	16 Feb 07	19.9	23.0	1.18	SA102-1081	1.34	0.0308	7.2	20.9	GMOSS	Sq
2016 CG18	28.5	16 Feb 05	17.6	1.1	1.07	SA102-1081	1.15	0.0004	4.9	48.6	GMOSN	Xe

Table 5
(Continued)

Object	H mag	Obs. Date (YY MM DD)	V mag (NEO)	Δ [LD]	Airmass (NEO)	Solar analog (SA)	Airmass (SA)	MOID (au)	Δv (km s ⁻¹)	Phase (deg)	Fac.	Taxon.
2016 CK29	25.6	16 Feb 09	20.0	18.9	1.15	SA102-1081	1.03	0.0354	5.9	11.5	GMOSN	Sr
2016 CL29	24.6	16 Feb 07	19.6	23.3	1.08	SA98-978	1.07	0.0324	7.8	22.1	GMOSN	Q
2016 CO29	24.9	16 Feb 07	20.2	25.7	1.08	SA98-978	1.08	0.022	5.5	19.2	GMOSN	L
2016 CS247	25.8	16 Feb 16	18.3	8.3	1.25	SA105-56	1.14	0.0117	4.5	24.3	DCT	S
2016 CU29	26.4	16 Feb 10	19.7	8.1	1.06	SA102-1081	1.07	0.0131	6.2	33.0	GMOSN	R
2016 EB1	25.2	16 Mar 06	18.8	14.5	1.45	SA102-1081	1.52	0.0134	7.1	8.7	GMOSS	Xc
2016 EB28	23.2	16 Mar 09	20.2	53.6	1.33	SA105-56	1.11	0.0039	6.6	15.9	GMOSS	Sq
2016 EL157	26.9	16 Mar 16	19.0	7.0	1.38	SA105-56	1.1	0.0074	6.3	9.0	GMOSN	Sq
2016 EN156	27.7	16 Mar 16	19.2	5.5	1.38	SA105-56	1.15	0.0019	5.0	8.6	GMOSN	K
2016 EQ1	25.9	16 Mar 10	20.5	20.0	1.11	SA102-1081	1.04	0.0053	4.7	8.5	GMOSN	T
2016 ES1	23.7	16 Mar 08	20.4	35.5	1.12	SA102-1081	1.1	0.0894	6.7	28.4	GMOSN	X
2016 FC	26.5	16 Mar 21	20.0	11.0	1.14	SA105-56	1.06	0.0001	4.8	23.4	GMOSS	Xc
2016 FL12	26.1	16 Apr 04	20.1	15.3	1.1	SA105-56	1.21	0.0243	4.7	12.8	GMOSN	Cb
2016 FW13	28.6	16 Apr 04	19.2	1.9	1.09	SA102-1081	1.04	0.0014	5.7	27.9	GMOSN	Xk
2016 GB222	26.3	16 Apr 19	19.4	6.3	1.24	SA107-998	1.08	0.0073	5.8	38.4	DCT	Q
2016 GV221	25.0	16 Apr 19	19.5	10.1	1.45	SA107-684	1.15	0.021	5.5	70.8	DCT	Q
2016 HB	24.3	16 Apr 19	19.2	16.3	1.49	SA107-684	1.22	0.012	5.5	41.1	DCT	Sa
2016 HN2	23.6	16 May 12	20.5	50.0	1.08	SA110-361	1.15	0.0611	6.1	28.0	GMOSN	Xk
2016 HQ19	23.8	16 May 27	20.2	24.9	1.11	SA110-361	1.18	0.0605	6.4	64.6	GMOSN	B
2016 JV	25.4	16 Jun 08	19.9	16.4	1.16	SA110-361	1.22	0.0366	5.9	45.9	GMOSS	B
2016 LG49	22.4	16 Jun 17	17.3	16.0	1.21	SA107-998	1.13	0.0334	10.5	44.1	DCT	Sq
2016 LO48	25.4	16 Jun 15	19.4	12.2	1.34	SA110-361	1.15	0.021	5.4	36.4	DCT	X
2016 NC1	25.3	16 Jul 16	18.9	8.0	1.21	SA112-1333	1.51	0.0187	5.8	52.1	GMOSS	A
2016 ND1	25.4	16 Jul 09	19.6	10.4	1.06	SA115-271	1.04	0.0147	5.4	58.2	GMOSN	Sq
2016 NM15	27.4	16 Jul 16	19.9	9.2	1.21	SA110-361	1.22	0.0111	4.2	4.8	GMOSS	B
2016 NN15	26.7	16 Jul 08	19.0	4.3	1.08	SA113-276	1.26	0.009	6.2	50.8	GMOSN	Sv
2016 NS	25.3	16 Jul 17	17.9	9.6	1.16	SA112-1333	1.01	0.0205	4.8	6.9	GMOSS	Xe
2016 PX8	27.0	16 Aug 12	20.0	7.6	1.21	SA93-101	1.1	0.0155	6.4	38.1	GMOSS	S
2016 QB2	24.2	16 Sep 10	19.8	36.1	1.06	SA115-271	1.07	0.0801	5.0	11.2	GMOSN	Xk
2016 QL44	25.1	16 Sep 09	20.0	26.4	1.17	SA115-271	1.13	0.0091	6.7	9.2	GMOSS	Sq
2016 QS11	25.8	16 Sep 15	19.4	12.4	1.23	SA115-271	1.23	0.0249	4.6	18.9	DCT	Xc
2016 RB1	28.2	16 Sep 07	15.3	0.5	1.22	SA93-101	1.15	0.0004	6.9	29.4	DCT	Xe
2016 RD20	24.6	16 Sep 27	20.3	31.9	1.06	SA93-101	1.11	0.072	6.6	12.0	GMOSN	Q
2016 RD34	27.4	16 Sep 15	19.9	3.4	1.29	SA93-101	1.11	0.0036	3.9	72.6	DCT	K
2016 RF34	24.4	16 Sep 15	18.5	7.7	1.05	HD28099	1.06	0.0107	5.7	71.4	DCT	Q
2016 RJ18	23.5	16 Sep 23	20.3	54.6	1.06	SA93-101	1.25	0.1091	5.9	14.1	GMOSN	A
2016 RL20	23.6	16 Sep 27	19.4	19.1	1.13	SA115-271	1.7	0.027	8.5	68.1	GMOSN	L
2016 RM20	26.2	16 Sep 24	20.1	7.8	1.23	SA115-271	1.71	0.0158	5.2	65.3	GMOSS	L
2016 RT33	23.9	16 Sep 15	19.7	26.6	1.23	SA115-271	1.15	0.0512	8.8	36.2	DCT	Sv
2016 RW	23.2	16 Sep 30	19.9	28.7	1.09	SA112-1333	1.24	0.0155	5.2	64.6	GMOSN	Q
2016 SA2	28.1	16 Sep 28	19.1	3.5	1.18	SA93-101	1.06	0.0017	4.5	22.6	GMOSS	Sq
2016 SW1	28.5	16 Sep 28	19.0	1.5	1.06	HD28099	1.09	0.002	4.7	74.8	GMOSN	Xe
2016 SZ1	26.4	16 Sep 29	19.7	6.1	1.03	HD28099	1.27	0.0108	6.0	66.9	GMOSN	L
2016 TB57	26.1	16 Oct 19	19.0	8.8	1.08	SA98-978	1.22	0.0	4.1	22.6	GMOSN	S
2016 TM56	26.7	16 Oct 22	18.7	5.3	1.12	SA93-101	1.12	0.0097	4.2	24.0	GMOSN	Sq
2016 XR23	25.3	16 Dec 23	20.0	15.0	1.08	SA93-101	1.22	0.003	5.2	40.8	GMOSN	Sq
2016 YC8	24.6	17 Jan 03	19.9	24.3	1.09	SA98-978	1.43	0.0006	5.5	26.4	GMOSN	Sr
2016 YH3	24.4	16 Dec 29	20.1	16.1	1.36	SA102-1081	1.24	0.0373	6.8	72.7	GMOSS	R
2016 YM3	26.9	16 Dec 29	19.3	4.4	1.36	SA102-1081	1.01	0.0091	5.6	64.7	GMOSS	X
2017 AR4	24.6	17 Jan 08	19.9	31.9	1.07	SA98-978	1.03	0.0354	5.4	5.0	GMOSN	Q
2017 AS4	26.7	17 Jan 08	16.8	1.7	1.19	SA102-1081	1.19	0.001	7.5	49.4	GMOSN	S
2017 AT4	26.7	17 Jan 08	19.2	11.0	1.07	SA98-978	1.0	0.028	4.5	2.9	GMOSN	Xc
2017 BK	24.0	17 Jan 24	19.2	15.9	1.08	SA105-56	1.12	0.0355	6.0	59.7	GMOSN	Sq
2017 BT	22.2	17 Jan 25	19.9	56.0	1.13	SA98-978	1.36	0.073	5.5	47.9	GMOSN	A
2017 BU	25.1	17 Jan 25	20.3	25.7	1.13	SA98-978	1.09	0.0229	5.8	20.5	GMOSN	T
2017 BW	23.3	17 Jan 31	18.2	19.7	1.16	SA102-1081	1.1	0.0103	4.7	23.8	GMOSS	Cgh
2017 CS	19.3	17 Jun 04	14.9	14.0	1.31	SA110-361	1.12	0.0049	6.9	62.8	DCT	C
2017 EH4	23.9	17 Mar 17	19.6	34.4	1.33	SA105-56	1.33	0.0644	5.7	8.1	DCT	Sa
2017 FJ	28.1	17 Mar 19	19.4	5.1	1.27	SA102-1081	1.18	0.0038	5.5	8.3	DCT	Sq
2017 FK	27.4	17 Mar 19	17.9	3.2	1.27	SA102-1081	1.07	0.0045	5.6	19.0	DCT	Sv
2017 JM2	24.1	17 May 14	17.0	5.9	1.39	SA105-56	1.23	0.0069	9.0	45.4	DCT	S
2017 QB35	29.3	17 Sep 02	18.1	1.4	1.29	SA93-101	1.18	0.0025	5.5	20.4	GMOSS	Q
2017 QG18	27.0	17 Sep 01	18.5	4.4	1.17	SA115-271	1.13	0.0045	5.2	26.2	GMOSS	Q

Table 5
(Continued)

Object	<i>H</i> mag	Obs. Date (YY MM DD)	<i>V</i> mag (NEO)	Δ [LD]	Airmass (NEO)	Solar analog (SA)	Airmass (SA)	MOID (au)	Δv (km s ⁻¹)	Phase (deg)	Fac.	Taxon.
2017 QR35	25.2	17 Sep 06	19.6	12.4	1.4	SA93-101	1.14	0.0163	5.5	46.0	GMOSN	Xc
2017 RB	28.0	17 Sep 05	19.1	4.0	1.47	SA93-101	1.26	0.0088	4.9	21.2	GMOSS	Q
2017 RB16	25.6	17 Sep 26	19.9	4.7	1.63	SA93-101	1.3	0.0103	6.5	105.4	GMOSS	Cg
2017 RS2	26.3	17 Sep 23	19.8	12.6	1.68	SA115-271	1.17	0.0101	4.2	11.3	GMOSS	Q
2017 RU2	25.9	17 Sep 20	19.6	7.5	1.13	SA115-271	1.33	0.0019	5.9	72.9	GMOSN	Sr
2017 RV2	26.3	17 Sep 20	20.0	12.9	1.07	SA93-101	1.5	0.0003	4.8	23.7	GMOSN	Xe
2017 VA15	25.1	17 Oct 19	17.8	8.1	1.06	HD28099	1.04	0.0182	5.7	22.9	DCT	X
2017 VC14	28.5	17 Nov 17	17.5	1.9	1.09	HD28099	1.05	0.001	6.3	11.1	GMOSN	Cg
2017 VG1	24.0	17 Nov 19	19.4	24.9	1.37	SA93-101	1.12	0.01	5.9	22.2	GMOSS	Xc
2017 VR12	20.5	18 Feb 25	15.8	14.5	1.29	SA105-56	1.33	0.0077	5.1	65.1	DCT	V
2017 VV12	28.0	17 Nov 16	19.6	2.4	1.22	SA102-1081	1.01	0.0007	5.2	78.7	GMOSN	Sr
2017 VY13	26.5	17 Nov 23	18.1	6.6	1.16	HD28099	1.2	0.005	5.9	8.7	DCT	Xc
2017 VZ14	25.0	17 Nov 23	16.2	3.9	1.16	HD28099	1.33	0.0069	5.9	24.4	DCT	Xc
2017 YF7	23.5	18 Jan 22	19.9	41.8	1.3	SA102-1081	1.28	0.1002	5.0	18.6	GMOSS	S
2017 YR3	25.3	18 Jan 08	20.3	22.0	1.18	SA98-978	1.12	0.007	5.0	26.1	GMOSS	Xk
2017 YW3	26.5	18 Jan 08	19.8	11.1	1.18	SA98-978	1.4	0.0069	4.2	21.0	GMOSS	Xe
2018 AF3	22.7	18 Jan 23	21.2	118.4	1.16	SA98-978	1.41	0.1091	5.6	5.4	GMOSS	L
2018 BG1	25.5	18 Jan 30	19.4	14.7	1.08	SA102-1081	1.17	0.0273	5.9	17.9	GMOSN	Sq
2018 DT	27.2	18 Feb 25	18.0	4.3	1.29	SA105-56	1.26	0.0105	4.1	10.9	DCT	Q
2018 DY3	25.6	18 Mar 10	19.1	5.5	1.28	SA105-56	1.01	0.0084	5.1	78.0	DCT	D
2018 EH	24.4	18 Mar 10	18.6	15.3	1.48	SA105-56	1.51	0.0101	6.6	25.1	DCT	Sq

Note. Δ corresponds to the object-observer distance at the moment of the observation expressed Lunar distance.

(This table is available in machine-readable form.)

Appendix B

Reflectance Spectra for the NEOs Observed by MANOS

Figure 12 shows postage stamp figures of all the spectra presented in this work.

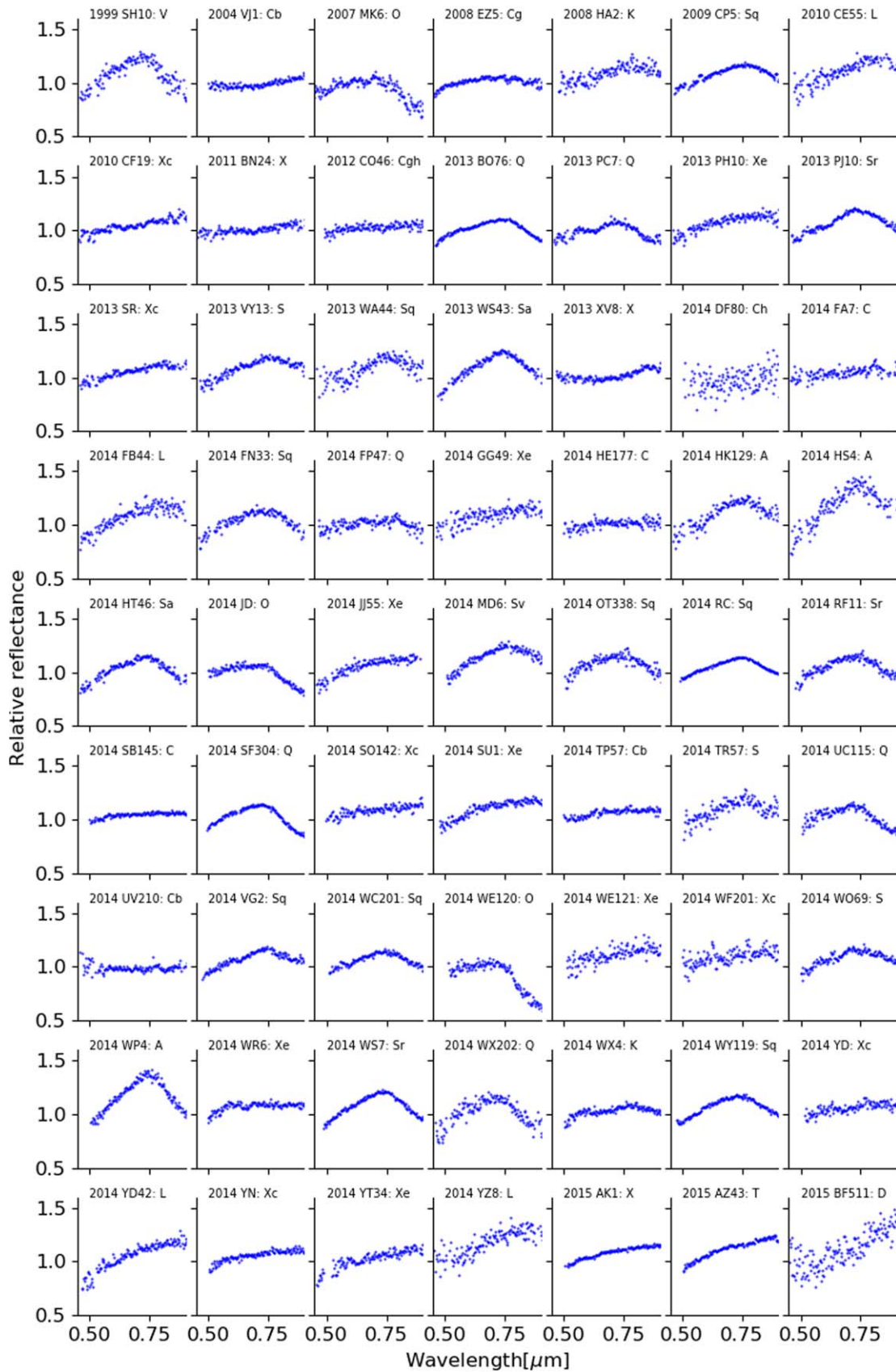


Figure 12. Obtained reflectance spectra (normalized at 0.55 μm) obtained in this work.

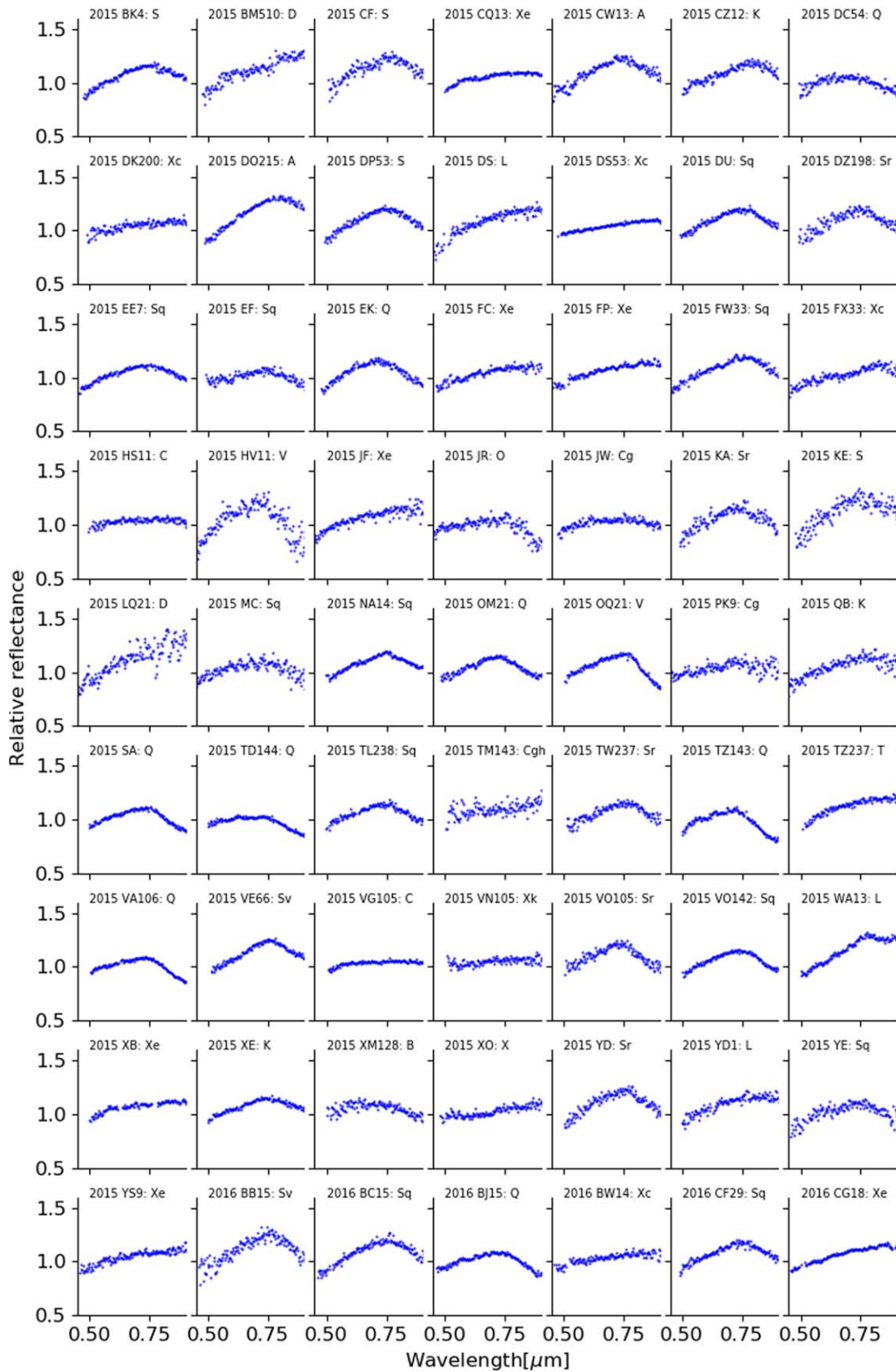


Figure 12. (Continued.)

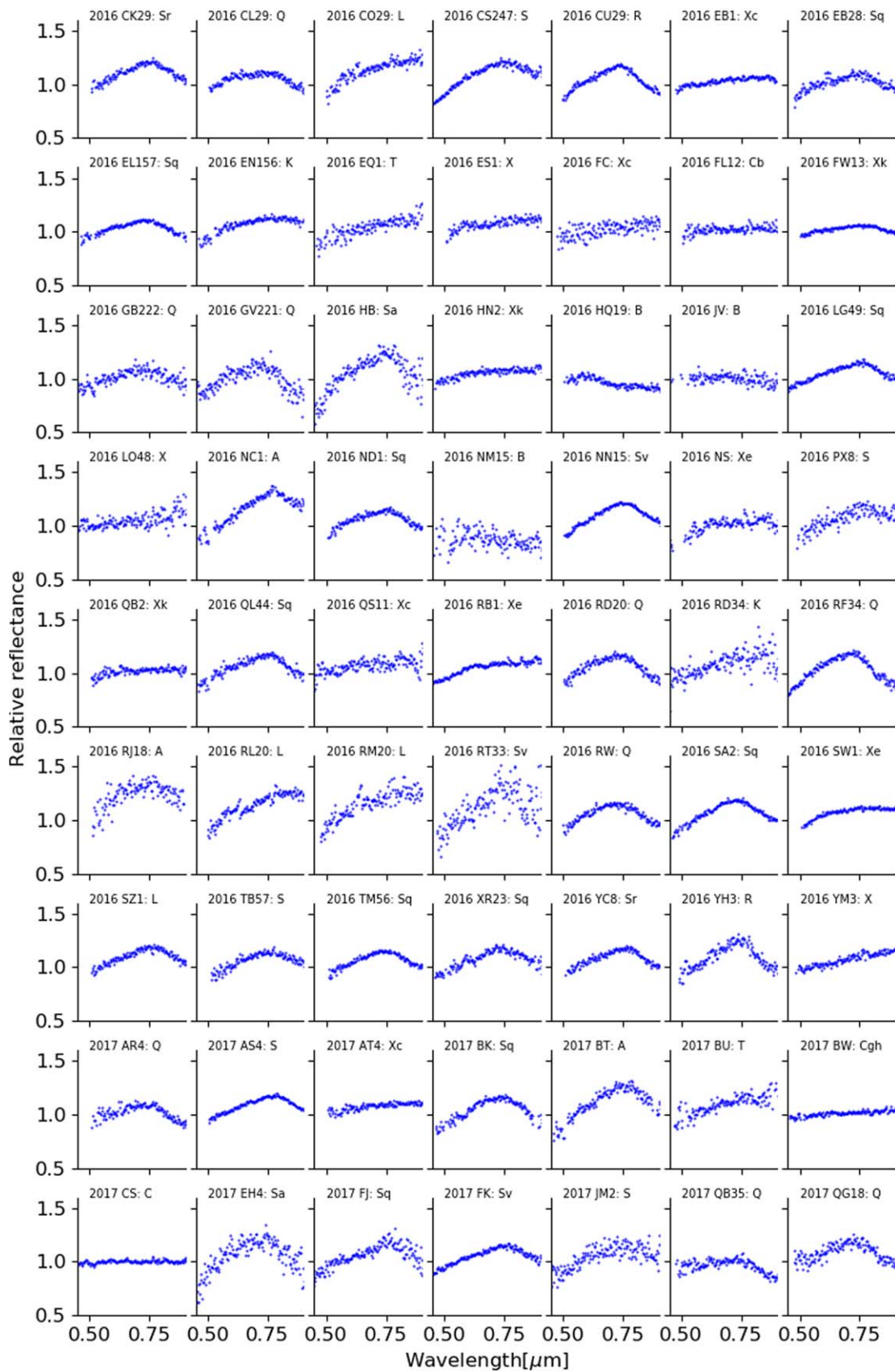


Figure 12. (Continued.)

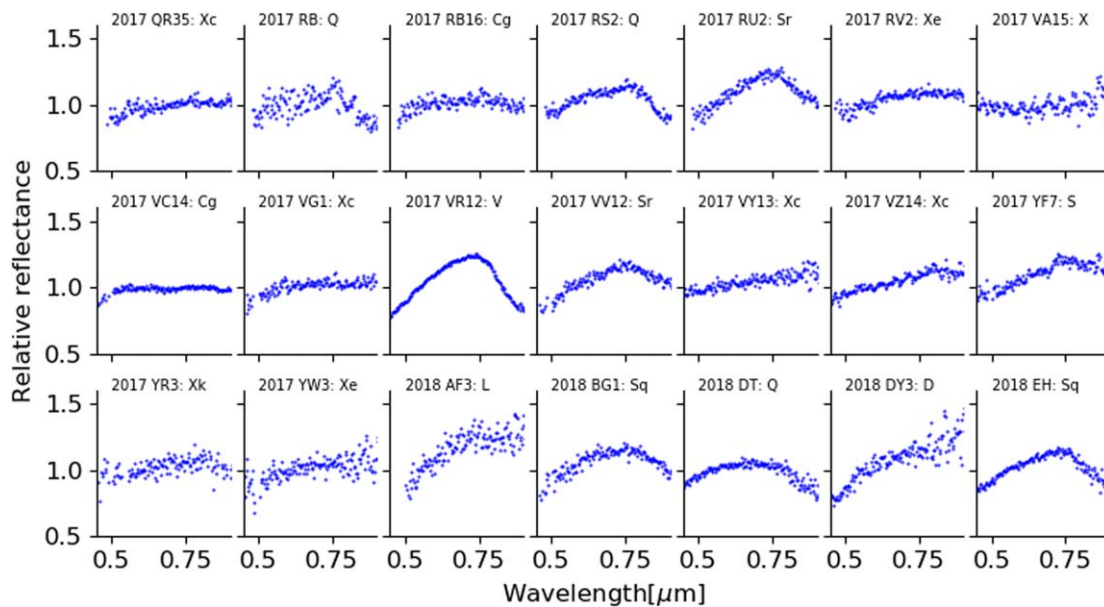


Figure 12. (Continued.)

ORCID iDs

Maxime Devogèle <https://orcid.org/0000-0002-6509-6360>

Nicholas Moskovitz <https://orcid.org/0000-0001-6765-6336>

Audrey Thirouin <https://orcid.org/0000-0002-1506-4248>

Cristina Thomas <https://orcid.org/0000-0003-3091-5757>

David Trilling <https://orcid.org/0000-0003-4580-3790>

Michael Mommert <https://orcid.org/0000-0002-8132-778X>

References

- Bida, T. A., Dunham, E. W., Massey, P., & Roe, H. G. 2014, *Proc. SPIE*, 9147, 91472N
- Binzel, R., DeMeo, F., Turtelboom, E., et al. 2019, *Icar*, 324, 41
- Binzel, R. P., Harris, A. W., Bus, S. J., & Burbine, T. H. 2001, *Icar*, 151, 139
- Binzel, R. P., Morbidelli, A., Merouane, S., et al. 2010, *Natur*, 463, 331
- Binzel, R. P., Rivkin, A. S., Stuart, J. S., et al. 2004, *Icar*, 170, 259
- Borisov, G., Christou, A., Bagnulo, S., et al. 2017, *MNRAS*, 466, 489
- Botke, W. F., Jr, Vokrouhlický, D., Rubincam, D. P., & Nesvorný, D. 2006, *AREPS*, 34, 157
- Burbine, T. H., & Binzel, R. P. 2002, *Icar*, 159, 468
- Bus, S. J., & Binzel, R. P. 2002, *Icar*, 158, 146
- Carry, B. 2012, *P&SS*, 73, 98
- Carvano, J. M., Lazzaro, D., Mothé-Diniz, T., Angeli, C. A., & Florczak, M. 2001, *Icar*, 149, 173
- Cellino, A., Bagnulo, S., Belskaya, I., & Christou, A. 2018, *MNRAS Letters*, 481, L49
- Chang, C.-K., Ip, W.-H., Lin, H.-W., et al. 2015, *ApJS*, 219, 27
- Chang, C.-K., Lin, H.-W., Ip, W.-H., et al. 2016, *ApJS*, 227, 20
- Chapman, C. R. 1996, *M&PS*, 31, 699
- Christou, A. A. 2013, *Icar*, 224, 144
- Davies, R. L., Allington-Smith, J. R., Bettess, P., et al. 1997, *Proc. SPIE*, 2871, 1099
- De León, J., Licandro, J., Serra-Ricart, M., Pinilla-Alonso, N., & Campins, H. 2010, *A&A*, 517, A23
- De Luise, F., Perna, D., Dotto, E., et al. 2007, *Icar*, 191, 628
- Delbó, M., Libourel, G., Wilkerson, J., et al. 2014, *Natur*, 508, 233
- DeMeo, F., & Carry, B. 2013, *Icar*, 226, 723
- DeMeo, F. E., Binzel, R. P., & Lockhart, M. 2014, *Icar*, 227, 112
- DeMeo, F. E., Binzel, R. P., Slivan, S. M., & Bus, S. J. 2009, *Icar*, 202, 160
- DeMeo, F. E., Polishook, D., Carry, B., et al. 2019, *Icar*, 322, 13
- Devogèle, M., Cellino, A., Borisov, G., et al. 2018, *MNRAS*, 479, 3498
- Dombard, A. J., Barnouin, O. S., Prockter, L. M., & Thomas, P. C. 2010, *Icar*, 210, 713
- Erasmus, N., Mommert, M., Trilling, D. E., et al. 2017, *AJ*, 154, 162
- Farnocchia, D., Chesley, S. R., Brown, P. G., & Chodas, P. W. 2016, *Icar*, 274, 327
- Farnocchia, D., Christensen, E., Gibbs, A., et al. 2018, AAS/DPS Meeting, 50, 111.02
- Granvik, M., Morbidelli, A., Jedicke, R., et al. 2016, *Natur*, 530, 303
- Granvik, M., Morbidelli, A., Jedicke, R., et al. 2018, *Icar*, 312, 181
- Hanuš, J., Delbó, M., Ďurech, J., & Alí-Lagoa, V. 2015, *Icar*, 256, 101
- Hanuš, J., Vokrouhlický, D., Delbo, M., et al. 2018, *A&A*, 620, L8
- Harris, A. W., & D'Abramo, G. 2015, *Icar*, 257, 302
- Hérique, A., Agnus, B., Asphaug, E., et al. 2018, *AdSpR*, 62, 2141
- Holsapple, K. A. 2007, *Icar*, 187, 500
- Jaumann, R., Williams, D., Buczkowski, D., et al. 2012, *Sci*, 336, 687
- Jenniskens, P., Shaddad, M., Numan, D., et al. 2009, *Natur*, 458, 485
- Krugly, Y. N., Belskaya, I., Shevchenko, V., et al. 2002, *Icar*, 158, 294
- Lucas, M. P., Emery, J. P., MacLennan, E. M., et al. 2019, *Icar*, 322, 227
- MacLennan, E. M., & Emery, J. P. 2018, *AJ*, 157, 2
- Maurel, C., Ballouz, R.-L., Richardson, D. C., Michel, P., & Schwartz, S. R. 2017, *MNRAS*, 464, 2866
- McEachern, F. M., Čuk, M., & Stewart, S. T. 2010, *Icar*, 210, 644
- McFadden, L. A., Gaffey, M. J., & McCord, T. B. 1985, *Sci*, 229, 160
- Michikami, T., Honda, C., Kawamura, M., et al. 2019, *Icar*, 331, 179
- Mommert, M., Trilling, D. E., Borth, D., et al. 2016, *AJ*, 151, 98
- Mountain, C. M., Kurz, R., & Oschmann, J. M. 1994, *Proc. SPIE*, 2199, 41
- Nakamura, T., Noguchi, T., Tanaka, M., et al. 2011, *Sci*, 333, 1113
- Navarro-Meza, S., Mommert, M., Trilling, D. E., et al. 2019, *AJ*, 157, 190
- Nesvorný, D., Jedicke, R., Whiteley, R. J., & Ivezić, Ž. 2005, *Icar*, 173, 132
- Ostro, S. J., Giorgini, J. D., & Benner, L. A. 2007, in IAU Symp. 236, NearEarth Objects, Our Celestial Neighbors: Opportunity and Risk, ed. G. B. Valsecchi, D. Vokrouhlický, & A. Milani (Cambridge: Cambridge Univ. Press), 143
- Perna, D., Barucci, M. A., Fulchignoni, M., et al. 2018, *P&SS*, 157, 82
- Polishook, D., Jacobson, S. A., Morbidelli, A., & Aharonson, O. 2017a, *NatAs*, 1, 0179
- Polishook, D., Moskovitz, N., Binzel, R., et al. 2016, *Icar*, 267, 243
- Polishook, D., Moskovitz, N., Binzel, R. P., et al. 2014, *Icar*, 233, 9
- Polishook, D., Moskovitz, N., Thirouin, A., et al. 2017b, *Icar*, 297, 126
- Robinson, M., Thomas, P., Veverka, J., Murchie, S., & Carcich, B. 2001, *Natur*, 413, 396
- Rozitis, B., MacLennan, E., & Emery, J. P. 2014, *Natur*, 512, 174
- Scheeres, D. 2018, *Icar*, 304, 183
- Scheeres, D. J., Hartzell, C. M., Sánchez, P., & Swift, M. 2010, *Icar*, 210, 968
- Sebring, T. A., Dunham, E. W., & Millis, R. L. 2004, *Proc. SPIE*, 5489, 658
- Shoemaker, E., & Helin, E. 1978, in NASA, Washington Asteroids, ed. D. Morrison & W. C. Wells (Washington, DC: NASA), 245
- Stuart, J. S., & Binzel, R. P. 2004, *Icar*, 170, 295
- sunshine, J., Connolly, H., McCoy, T. J., Bus, S., & La Croix, L. 2008, *Sci*, 320, 514

- Tancredi, G., Roland, S., & Bruzzone, S. 2015, *Icar*, 247, 279
- Thirouin, A., Moskovitz, N., Binzel, R., et al. 2016, *AJ*, 152, 163
- Thirouin, A., Moskovitz, N. A., Binzel, R. P., et al. 2018, *ApJS*, 239, 4
- Tholen, D. J. 1984, PhD thesis, Univ. Arizona
- Thomas, C. A., Rivkin, A. S., Trilling, D. E., Enga, M.-t., & Grier, J. A. 2011a, *Icar*, 212, 158
- Thomas, C. A., Trilling, D. E., Emery, J., et al. 2011b, *AJ*, 142, 85
- Trilling, D., Valdes, F., Allen, L., et al. 2017, *AJ*, 154, 170
- Turrini, D., Svetsov, V., Consolmagno, G., Sirono, S., & Pirani, S. 2016, *Icar*, 280, 328
- Van Dokkum, P. G. 2001, *PASP*, 113, 1420
- Walsh, K. J., Richardson, D. C., & Michel, P. 2008, *Natur*, 454, 188
- Warner, B. D., Harris, A. W., Vokrouhlický, D., Nesvorný, D., & Bottke, W. F. 2009, *Icar*, 204, 172